

# Modelling Present and Future Climate in the Mediterranean Sea: A Focus on Sea-Level Change

**Gianmaria Sannino** (✉ [gianmaria.sannino@enea.it](mailto:gianmaria.sannino@enea.it))

ENEA Casaccia Research Centre: ENEA Centro Ricerche Casaccia <https://orcid.org/0000-0002-3985-9432>

**Adriana Carillo**

ENEA Casaccia Research Centre: ENEA Centro Ricerche Casaccia

**Roberto Iacono**

ENEA Casaccia Research Centre: ENEA Centro Ricerche Casaccia

**Ernesto Napolitano**

ENEA Casaccia Research Centre: ENEA Centro Ricerche Casaccia

**Massimiliano Palma**

ENEA Casaccia Research Centre: ENEA Centro Ricerche Casaccia

**Giovanna Pisacane**

ENEA Casaccia Research Centre: ENEA Centro Ricerche Casaccia

**MariaVittoria Struglia**

ENEA Casaccia Research Centre: ENEA Centro Ricerche Casaccia

---

## Research Article

**Keywords:** Mediterranean Sea climate, MED16, altimetric observations, RCP8.5

**Posted Date:** July 1st, 2021

**DOI:** <https://doi.org/10.21203/rs.3.rs-653703/v1>

**License:**   This work is licensed under a Creative Commons Attribution 4.0 International License. [Read Full License](#)

---

**Version of Record:** A version of this preprint was published at Climate Dynamics on January 21st, 2022. See the published version at <https://doi.org/10.1007/s00382-021-06132-w>.

# Abstract

We present results of three simulations of the Mediterranean Sea climate: a hindcast, a historical run, and a RCP8.5 scenario simulation reaching the year 2100. The simulations are performed with MED16, a new, tide-including implementation of the MITgcm model, which covers the Mediterranean - Black Sea system with a resolution of  $1/16^\circ$ , further increased at the Gibraltar and Turkish Straits.

Validation of the hindcast simulation against observations and numerical reanalyses has given excellent results, proving that the model is also capable of reproducing near-shore sea level variations. Moreover, the spatial structure of the elevation field compares well with altimetric observations, especially in the Western basin, due to the use of improved sea level information at the Atlantic lateral boundary and to the adequate treatment of the complex, hydraulically driven dynamics across the Gibraltar Strait.

Under the RCP8.5 future scenario, the temperature is projected to generally increase while the surface salinity decreases in the portion of the Mediterranean affected by the penetration of the Atlantic stream, and increases elsewhere. The warming of sea waters results in the partial inhibition of deep-water formation.

The scenario simulation allows for a detailed characterization of the regional patterns of future sea level, arising from ocean dynamics, and indicates a relative sinking of the Mediterranean with respect to the Atlantic more pronounced than the current one. Explicit tidal forcing and an accurate resolution of the Gibraltar Strait are proved to be key features in the designing of numerical simulations for the Mediterranean Sea.

## 1. Introduction

Future sea level rise (SLR) constitutes a threat for the coastal environment and economies, which is liable to be further exacerbated by the superposition of waves, atmospheric surge, and tides. Climate scientists are therefore becoming more and more committed to improve projections of SLR as to both resolution and accuracy, and to reduce current uncertainties, at the same time increasing our understanding of such a challenging scientific problem and enabling more accurate risk assessments. The latter, in particular, suffer from the difficulty in accounting for the cascading effects from sea-level rise to actual coastal impacts, across a range of spatial and temporal scales that demand complex and differentiated approaches (Thiéblemont et al., 2019). Likewise, the lack of comprehensive projections of extreme sea levels (ESL) that include mean sea level (MSL), tides, waves, and storm surges is lamented by Vousdoukas et al. (2017), who present a first attempt to provide an impact-oriented, regional-scale evaluation of ESL for the European shoreline. Their effort, albeit still inadequate for the design of specific measures, can nevertheless help highlight vulnerabilities and emerging research issues. As a matter of fact, the authors denounce the limitations inherent to their approach, mainly arising from the inadequacy of the regional atmospheric projections available at the time, as well as those of the projections derived from coupled global OGCMs. In addition, they highlight that explicitly solving the nonlinear interactions between waves, storm surge, and tides should be a key element of any future effort to reliably model ESL, rather than continuing to resort to linear combinations of the ESL components resulting from independent simulations.

Besides being highly vulnerable to SLR due to the potentially disruptive impacts on its coastal economies (Jeftic et al., 1992), the Mediterranean basin is especially challenging from the scientific perspective, due to the

inherent diversity of its geological history and the peculiar and complex features of its marine circulation and environment. In addition to the local dynamics and geological processes, interacting over a broad spectrum of scales, sea level in the basin is also constrained by the water mass exchange across the Strait of Gibraltar, which, in fact, regulates the hydraulic jump between the Mediterranean and the Atlantic Ocean and influences how sea level rise in the Atlantic is transmitted into the Mediterranean. In its turn, the connection with the Black Sea, through the Dardanelles, Sea of Marmara and the Bosphorus, couples the basin hydrology to the land-based hydrological cycle of a vast portion of continental Europe. Nevertheless, despite the recognized inability of coarse resolution GCMs to accurately represent the highly non-linear, small-scale processes in marginal seas such as the Mediterranean (Slangen et al., 2017a; Marcos and Tsimplis, 2008), the global stereodynamic (following the terminology proposed by Gregory et al., 2019) sea-level projections for the Atlantic area near Gibraltar, are still often used to estimate the basin's internal sea level (Thiéblemont et al., 2019).

At the global scale, the question is still open whether the strong trends observed in the last 25 years through satellite altimetry are part of longer-term tendencies, or reflect more recent changes in the atmosphere-ocean coupled system. Recent work by Dangendorf et al. (2019) provides evidence that the global trend accelerated at the end of the 1960s, and indicates that the resulting acceleration in the global sea level rise is linked to modifications of the southern hemispheric westerlies, leading to warming and circulation changes in the southern world ocean. Other factors have also been shown to play a key role, such as the change of terrestrial water storage, and the melting of ice sheets and glaciers, which has significantly increased in the last decades (see, e.g., Shugar et al., 2020, which focuses on the growth of glacial lakes, and King et al., 2020, where the mass loss from the Greenland Ice Sheet is analyzed). The work by Frederikse et al. (2020) provides a thorough review of the various contributions and their relative weight.

As to future scenarios, since 1995 the coordinated worldwide CMIP effort (Coupled Model Intercomparison Project) has provided constantly updated projections of future sea level rise using earth-system models, to which the contributions from continental glaciers and geologic processes are added offline. The Phase 5 models (CMIP5) used for the fifth Intergovernmental Panel on Climate Change (IPCC) assessment report (AR5, IPCC 2013) project a global sea level rise between 26 and 97 cm (overall likely range) at the end of this century, depending on the climate scenario, with pretty large inter-model spread. Such estimates were revised in the 2019 Special Report on the Ocean and Cryosphere in a Changing Climate (SROCC), which assigns medium confidence to a likely range between 29 cm and 110 cm (IPCC, 2019). For the area of the North Atlantic in proximity of the Strait of Gibraltar, projections can range from about 40 cm to over 100 cm for the most pessimistic RCP8.5 scenario, with an ensemble mean of about 80 cm, and approximately from 30 cm to 80 cm for the intermediate RCP4.5 scenario, with an ensemble mean of 60 cm (Vousdoukas et al., 2017). On the other hand, Slangen et al., 2014 presented regional sea-level projections and their associated uncertainties up to the end of the 21st century, by combining model- and observation-based regional contributions of land ice, groundwater depletion and glacial isostatic adjustment, and CMIP5 projections of the changing ocean circulation, increased heat uptake and atmospheric pressure patterns, also accounting for gravitational effects due to mass redistribution, ending up with an estimate of about 70 cm for the Mediterranean Basin. However, while concluding that regional variations in sea-level can significantly differ from the global mean (up to 30% above and 50% below) and that the land ice contribution dominates the overall uncertainty, they also stressed the need for dedicated regional downscaling of each global climate scenario.

In general, the inherent uncertainty in SLR projections has induced researchers to adopt a variety of alternative estimates in their impact assessments. Thiéblemont et al. (2019) analyze the effects of a median estimate of about 80 cm and two different high-end scenarios, resulting from two extreme estimates for the sea-level equivalent of melting glaciers (i.e. the the upper limit of the likely range and the “worst model” projections). Antonioli et al. (2017), while reviewing possible alternative ranges for the projected high-end SLR at 2100, use the 530–970 mm interval reported in the IPCC AR5, and Rahmstorf’s semi-empirical estimate of about 1.400 mm (Rahmstorf, 2007). Improved projections from the next generation of global models are expected by 2022, when the next IPCC assessment is to be delivered. However, as remarked above, the spatial resolution of current global models is not sufficient to provide realistic estimates of local sea level rise in areas, such as the Mediterranean, where crucial processes are far from being explicitly resolved, and hardly allow a reliable parameterization (Sannino et al., 2009).

Adloff et al. (2018) recently discussed the complexity inherent to projecting sea level in the Mediterranean, and analyzed the performances of four different regional hindcast simulations of the basin circulation (period 1980–2012), driven by realistic atmospheric forcing. The incorporation of improved sea level information at the Atlantic lateral boundary was found to significantly enhance the reliability of results, confirming that the correct representation of the interactions between the two basins is an important requirement for a successful numerical simulation. However, an adequate treatment of the complex, hydraulically driven dynamics across the Strait of Gibraltar was still missing, as well as a more refined treatment of the exchange between the Mediterranean Sea and the Black Sea through the Dardanelles Strait, at the model eastern boundary. In addition, model performances were mostly evaluated by computing basin averages, while altimeter data series clearly indicate that sea level rise has not been homogeneous in the basin over the last decades. By analyzing altimeter data over a 25 years period (1993–2017), Mohamed et al. (2019) showed that the observed increase in the average sea level anomaly (SLA) has been quite different in different sub-basins, ranging from a minimum of 1.95 mm/year, in the Ionian Sea, to a maximum of 3.73 mm/year, in the Aegean Sea. At a broader scale, the SLA positive trend appears to be significantly stronger in the Levantine basin than in the Western Mediterranean Sea, as well as characterized by distinctive features, with a fairly regular linear increase in the Western Mediterranean Sea, possibly attributable to the Atlantic contribution, and a more complex behavior in the Levantine basin. The latter, in particular, is liable to be influenced by the evolution of the Eastern Mediterranean Transient (EMT), the dramatic event occurred in the eastern Mediterranean at the beginning of the 1990s (Roether et al., 1996; Klein et al., 1999, Theocharis et al., 2002). The difficulty in separating climate-change-induced variations from the local circulation variability is therefore evident, as well as the role played by small-scale features, either attributable to internal variability or determined by atmospheric forcing, in generating long-lasting differences across the Mediterranean sub-basins, amplifying or mitigating the effects of global sea level rise.

Prompted by these considerations, we developed a regional ocean model for the long-term simulation of the Mediterranean Sea circulation (hereinafter MED16) which we used to obtain accurate projections of the Mediterranean sea level. The model represents the climate version of the high-resolution, tide-including ocean model described in Palma et al. (2020). The two models share the same computational domain, which includes the Black Sea, thus allowing to consistently compute water exchanges at the Dardanelles Strait and to avoid any ad hoc assumption at the Mediterranean eastern boundary. The climate version necessarily uses a coarser horizontal grid with respect to its operational counterpart, yet resolution is significantly increased in

critical regions such as the Gibraltar, Dardanelles, and Bosphorus Straits. The explicit, high-resolution representation of inter-basin water exchanges at the boundaries constitutes a unique, distinguishing feature of the present implementation.

In the following, we analyze the hindcast of the Mediterranean circulation forced by the SMHI-RCA4 regional downscaling of the ECMWF ERA-Interim reanalysis data (Dee et al. 2011), and the historical and RCP8.5 scenario forced by the SMHI-RCA4 regional downscaling of the HadGEM2-ES global projection (Collins et al., 2011). The overall basin-scale model performance is assessed through comparison with observations and reanalysis data, with special focus on the model ability to reliably represent the local sea level height. In particular, comparison with data from tide gauges allows us to evaluate the model performance in coastal regions, where the impacts of sea level rise really affect human communities and economies, and need to be specifically assessed.

The paper is organized as follows. The main characteristics of the model and of its implementation are described in Sect. 2, whereas Sect. 3–5 are devoted to the detailed analysis of the simulations performed. In particular, Sect. 3 presents a validation of the hindcast and historical simulations in terms of transports at the main straits, hydrology, and circulation, obtained through comparison with observations and numerical reanalyses. The corresponding sea-level reconstructions are discussed in Sect. 4, and validated using satellite altimeter data and coastal tidal gauge observations. Section 5 then describes the results of the scenario simulation, highlighting future changes in the basin hydrology and circulation, and discussing the projected sea-level. Finally, conclusions are drawn in Sect. 6.

## 2. Data And Methods

In order to produce the downscaled Mediterranean sea-level field under present climate (1980–2005) and the RCP8.5 future scenario (2006–2100), the MED16 model was forced using the correspondent regional downscaling experiments performed with the SMHI-RCA4 atmospheric model (Strandberg et al., 2014), alternatively constrained by a) the ERA-Interim reanalysis data, for the hindcast simulation, b) the HadGEM2-ES global model (Collins et al., 2011) for the historical simulation, and c) the HadGEM2-ES RCP8.5 for the future scenario. The current section describes in detail the atmospheric data used (Sect. 2.1) and the MED16 model characteristics and specific setup (Sect. 2.2).

### 2.1 Atmospheric forcing

The atmospheric forcing is derived from the dynamically downscaled regional atmospheric fields produced by the Rossby Centre regional atmospheric model RCA4 (Strandberg et al., 2014), at  $0.11^\circ$  resolution (i.e. approx. 12.5 km grid spacing), over the EURO-CORDEX domain (Giorgi et al., 2009), whose boundary conditions are either provided by the ERA-Interim reanalysis, or by the atmospheric component of the CMIP5 global model HadGEM2-ES, which is commonly used for downscaled sea-level projections (Hermans et al., 2020). The hindcast experiment covers the period 1981–2010, the historical experiment covers the period 1981–2005, while the RCP-8.5 scenario spans years from 2006 to 2100. Up to 2005, observed greenhouse gas concentrations have been prescribed, which are then substituted by those indicated by Meinshausen et al. (2011) for the future business-as-usual scenario RCP8.5.

To reproduce the surface heat fluxes, shortwave radiation from the atmospheric models is imposed, whereas the wind stress and the other heat flux components are computed via bulk formulas considering the sea surface temperature, the winds at 10 m height, the dry air temperature and the air pressure at 2 m, and the relative humidity as inputs. In particular the long-wave radiation is computed according to the formula proposed by Bignami et al. (1995), while the latent heat flux, the sensible heat flux and wind stress are computed according to the Large and Yeager (2004) bulk formula. Cloud cover is taken from the atmospheric model. The net freshwater flux is computed as precipitation (taken from the atmospheric model) minus evaporation (computed from the latent heat). To reduce salinity drift in the hindcast simulation the sea surface salinity (SSS) is restored toward the MEDHYMAP monthly climatology (Jordà et al., 2017a) at a timescale of two days over the topmost model layer of 2 m thickness. At the surface, the model is forced by 6-hourly wind, and 3-hourly surface pressure, heat and freshwater fluxes computed via bulk formulae. The fresh water flux is prescribed in conjunction with the non-linear free surface numerical scheme.

## 2.2 The regional ocean model MED16

The numerical ocean model MED16 used to simulate the downscaled sea level is the updated version of the Mediterranean ocean model developed by Sannino et al. (2015). It is based on the MITgcm kernel developed by Marshall et al. (1997a, b), and solves the Navier-Stokes equations under the Boussinesq approximation for an incompressible fluid. In the present study, the hydrostatic version of the model has been implemented, using a finite-volume spatial discretization on a staggered Arakawa-C grid, partial step topography, rescaled vertical height ( $z^*$ ) coordinate (Adcroft and Campin 2004), and an implicit non-linear free surface formulation (Campin et al. 2004). The source code and documentation are available at the following web site: <https://github.com/MITgcm/MITgcm> (last access: 20 April 2021).

Model bathymetry for both the Mediterranean and the Black Sea was derived from the European Marine Observation and Data Network (EMODnet) 2016 dataset (<https://www.emodnet-bathymetry.eu>), while the high-resolution digitalized chart of Sanz et al. (1991) provided data for the SoG, and the high-resolution bathymetry for the Bosphorus and Dardanelles Straits was made available by Erkan Gökaşan (Gökaşan et al. 2005, 2007), with the permission of the Turkish Navy, Navigation, Hydrography and Oceanography Office. The datasets were combined through a bilinear interpolation on the computational grid, followed by manual check for isolated grid points, islands, and narrow passages (see Sannino et al., 2015, 2017). Both equilibrium tide (i.e. the generating potential is incorporated in the momentum equations as a body force) and tide propagating from the Atlantic Ocean through the Atlantic open boundary, are explicitly applied as in Naranjo et al. 2014, Sannino et al. 2015, and Palma et al. 2020. The equilibrium tide is composed of four tidal components: M2, O1, S2, K1, the semidiurnal and diurnal principal lunar tides, the principal semidiurnal solar tide, and diurnal lunisolar declination tide, respectively. The tidal values used to prescribe the Atlantic tide are derived from the OTIS global tide inverse model (Egbert and Erofeeva, 2002). Differently from the model configuration of Naranjo et al. 2014, and Sannino et al. 2015 the updated version used in this study includes the Black Sea that is interactively connected to the Mediterranean Sea through the Turkish Straits (Dardanelles and Bosphorus). The model domain therefore covers the whole Mediterranean-Black Sea system and a small part of the Atlantic Ocean west of the Strait of Gibraltar (SoG hereafter), whose western limit corresponds to the only open-boundary condition prescribed. The horizontal computational grid has a uniform resolution of  $1/16^\circ$  (about 7 km), which is significantly increased in correspondence of the three straits where higher resolution is needed to

reliably represent the local dynamics, i.e., the SoG (maximum resolution of about 200 m), and the Dardanelles and Bosphorus Straits, where a smoothly varying refinement in the latitudinal and longitudinal directions allows to reach a maximum resolution of  $1/200^\circ$  (about 555 m) (Fig. 1). The vertical domain is discretized using 100 z-levels, with grid spacing increasing from 2 m near the surface to 62 m at a depth of 1500 m; below 1500 m a uniform grid spacing of 62 m is used down to the sea floor. The time-step used is one minute. To calculate the vertical eddy viscosity and diffusivity coefficients, we used the 1.5 order Turbulent Kinetic Energy (TKE) closure scheme by Gaspar et al., 1990, adapted from the atmospheric case developed by Bougeault and Lacarrere (1989). The background vertical eddy viscosity and diffusivity were set to  $1.5 \cdot 10^{-6} \text{ m}^2/\text{s}$  and  $10^{-7} \text{ m}^2/\text{s}$ , respectively. The maximal value of diffusivity allowed to be generated by the turbulence scheme is  $100 \text{ m}^2/\text{s}$ , in order to let it handle unstable vertical stratification and avoid the use of an enhanced vertical mixing parameterization. A spatial-dependent horizontal viscosity is obtained from the turbulence closure scheme by Leith (1968). Differently from the well-known scheme by Smagorinsky (1963), Leith's scheme focuses on resolving the direct enstrophy cascade (cascade towards the smaller scales) that is characteristic of 2D turbulence (Fox-Kemper and Menemenlis, 2008). A constant horizontal diffusivity coefficient ( $2 \text{ m}^2 \text{ sec}^{-1}$ ) is applied with a laplacian operator for the tracers (T,S). The no-slip conditions were used at the lateral and bottom solid boundaries, along with a quadratic bottom drag. The latter is calculated as a function of the velocity close to the bottom, with a dimensionless coefficient of 0.0025. The selected tracer advection scheme is a third-order direct space-time flux limited scheme.

As the low spatial resolution of the global model did not allow an accurate representation of the dynamics within the Strait of Gibraltar, the Mediterranean basin was completely detached from the Atlantic Ocean in the global simulation, by artificially closing the Strait. The Mediterranean was therefore virtually represented as a lake in the global projection, thus impairing its use to initialize the regional ocean simulation. Initial conditions (namely temperature and salinity) were thus derived from MEDHYMAP climatological data. To reduce spurious drift, MED16 was spun-up 35 years, using the hindcast forcing for the 1980–1986 period in a five-time loop. The span-up model was then used as initial condition for both historical and hindcast simulations.

At the Atlantic open boundary, consistently with the surface atmospheric forcing, the hindcast simulation was forced with ORAS4 global reanalysis (Balmaseda et al. 2013), while for historical and RCP8.5 scenario simulations monthly data from the HadGEM2-ES global model were used. In particular, the lateral boundary conditions consist of monthly mean temperature, salinity and sea surface height (SSH) which are interpolated onto the MED16 grid. Temperature and salinity are applied through a 3D relaxation with a relaxation time varying linearly from 2 hours at the western limit of the domain to 30 days over the first 30 grid points. The prescribed SSH on the Atlantic box includes different contributions depending on the forcing. For the hindcast simulation, the prescribed ORAS4 SSH includes sea level contributions from ice sheet mass loss, glaciers ice melt, changes in land water storage, as well as global thermal expansion. As ORAS4 underestimates the regional SSH seasonal cycle in the near Atlantic region compared with the multi-satellite products provided by the Climate Change Initiative (CCI-SLA doi:10.5270/esa-sea\_level\_cci-MSLA-1993\_2013-v\_1.1-201412), we have applied a 12-month correction based on the difference between CCI-SLA and ORAS4 as described in Adloff et al. (2018). For both historical and scenario simulations, the prescribed SSH includes the dynamic sea level (DSL) and the global mean thermal expansion. DSL is the height of the ocean with respect to the time-invariant geoid that is determined by the dynamical balance associated with ocean density and circulation.

DSL includes the regional variability of dynamic topography changes due to water mass advection, thermohaline circulation and to the wind-driven circulation (Gill and Niller 1973) and are part of the standard output in the CMIP5 simulations (variable *zos*). *zos* was initially de-drifted by removing the linearly fitted HadGEM2-ES control run (which is forced by non-evolving pre-industrial conditions) from each grid point individually. This step removes any artificial signals associated with ongoing spin-up deep ocean and/or limitations in the representation of energy conservation in the model domain, as discussed by Sen Gupta et al. (2013). As the ocean component of HadGEM2-ES is based on the Boussinesq approximation and conserves volume rather than mass (Greatbatch, 1994), the value of *zos* was further corrected (at each time step and grid point) by subtracting its time dependent global mean. This correction guarantees that the resulting sea-level patterns only reflect fluctuations due to the joint effects of ocean density and circulation (Gregory et al., 2019) and thus, it is comparable to those resulting from non-Boussinesq models (Losch et al., 2004; Griffies and Greatbatch, 2012).

The corresponding global thermal expansion time series (variable *zostoga*) was also corrected for control drift by removing a quadratic fit to the control run's thermal expansion time series before being added to the detrended and zero global mean *zos* field. The resulting sea level variable was then used as SSH lateral boundary condition for the MED16 historical and scenario simulations. As in Naranjo et al 2014, Sannino et al 2015, and the higher resolution Mediterranean version of Palma et al (2020), SSH and the additional 4 tidal constituents were directly prescribed at the western open boundary.

The remaining sea level components for the historical and scenario simulations, namely the surface mass balance and dynamic ice sheet contributions from Greenland and Antarctica, the glacier and land water storage contributions, and the Glacial Isostatic Adjustment (GIA), were extracted from the Integrated Climate Data Center (ICDC) at Hamburg University (<https://icdc.cen.uni-hamburg.de/en/ar5-sl.html>), interpolated on the MED16 grid, and added offline. The ICDC dataset is based on the ensemble mean of CMIP5 climate models that were used in the regional sea-level projections of the AR5 (Church et al. 2013a) of the IPCC. ICDC provides data on a global grid at  $1^\circ \times 1^\circ$  spatial resolution for different RCP scenarios. In this study, we used central estimation data of the RCP8.5 ensemble mean.

River discharge at the river outlets is prescribed by transporting the daily total runoff computed by the forcing atmospheric regional model, along the river network of the WBMplus model (Vörösmarty et al. 1998; Wisser et al. 2008, 2010), by means of a Muskingum-Cunge type scheme that solves the Saint-Venant flow equations (Ponce 1994). Only for rivers discharging in the Black Sea, the so computed discharge was bias-corrected to reproduce monthly climatological values reported in the literature (Kara et al. 2008).

### 3. Model Validation

Before analysing the model sea level reconstructions (see Sect. 4), here we perform a first validation of the hindcast and historical runs. In particular, we compare the simulated water transports at the straits and the Mediterranean hydrology and circulation with the observations, and with the results of a recent reanalysis of Mediterranean water properties by Escudier et al (2020). The latter is a product from the Copernicus CMEMS database (<http://marine.copernicus.eu>) that covers the period 1987–2019, and results from the assimilation of temperature and salinity vertical profiles and satellite Sea Level Anomaly along track data into a numerical

system, consisting of the Nucleus for European Modelling of the Ocean (NEMO), and of a variational data assimilation scheme (OceanVAR).

As our focus is on the Mediterranean Sea, we will mainly show results for this basin, and report the projected water exchanges at the Dardanelles as a boundary condition, determined by the Black Sea effectively acting as a reservoir. Nevertheless, it is worth noting that the model correctly reproduces the permanent basin-scale, cyclonic boundary current that characterizes the Black Sea circulation.

### 3.1 Transports at the main straits: Gibraltar, Dardanelles, Bosphorus

The explicit treatment of water inflow and outflow at the open boundary of the Mediterranean Sea, coupled with explicit tidal forcing, allows to realistically constrain the mass, energy and momentum exchanges with adjacent basins, as well as to finely modulate the temperature and salinity properties of either flow, in both time and space (see Sannino et al, 2015, for a detailed description). Table 1 reports the simulated averaged long-term (1980–2011) transports across the main straits (Gibraltar, Dardanelles, and Bosphorus), for both the hindcast and historical experiments. The sections used to compute transports are located at 5.4° W for the SoG, at 26.2° E for the Dardanelles Strait, and at 41° N for the Bosphorus Strait. Transport is positive for an eastward or northward flow.

Table 1

Averaged water transport (in  $\text{m}^3/\text{s} \times 10^3$ ) through the Strait of Gibraltar, Dardanelles and Bosphorus over the period 1982–2011. [Mean value and Monthly standard deviation]. A negative flow is directed towards the Atlantic for the Strait of Gibraltar, and into the Mediterranean Sea for the Dardanelles and the Bosphorus

<b>NET</b>	<b>Gibraltar</b>	<b>Dardanelles</b>	<b>Bosphorus</b>
<b>Hindcast</b>	60 ± 90	-2 ± 7	-1 ± 8
<b>Historical</b>	60 ± 60	-4 ± 9	-4 ± 9
<b>INFLOW</b>	<b>Gibraltar</b>	<b>Dardanelles</b>	<b>Bosphorus</b>
<b>Hindcast</b>	930 ± 90	15 ± 2	5 ± 4
<b>Historical</b>	1080 ± 80	14 ± 3	5 ± 3
<b>OUTFLOW</b>	<b>Gibraltar</b>	<b>Dardanelles</b>	<b>Bosphorus</b>
<b>Hindcast</b>	-870 ± 100	-17 ± 7	-7 ± 4
<b>Historical</b>	-1020 ± 70	-18 ± 7	-9 ± 6

For the hindcast simulation the net average transport of 0.06 Sv at the Strait of Gibraltar results from a mean inflow from the Atlantic of about 0.93 Sv and a Mediterranean outflow of about - 0.87 Sv, and compares favorably with previous estimates based on the evaluation of the Mediterranean long-term hydrological deficit (E-P-R), which needs to be compensated by the excess Atlantic inflow. As a matter of fact, a recent work by

Jordà et al. (2017b) reports values ranging from 0.04 Sv (Soto-Navarro et al., 2010) to 0.06 Sv (Boutov et al., 2014), while proposing an intermediate estimate of  $0.05 \pm 0.03$  Sv based on an independent evaluation of the hydrological budget, and a lower bound of 0.03 Sv deriving from the optimal interpolation (OI) of Acoustic Doppler Current Profiler (ADCP) and tide gauge data. The projected average outflow is also close to previous estimates reported in the literature, which range from  $-0.67$  Sv (Tsimplis and Bryden, 2000) to  $-0.97$  Sv (Candela 2001), and include the  $-0.78$  Sv estimate of Sánchez Román et al. (2009), obtained by combining three years of ADCP observations and numerical modelling. A higher estimated value of  $-0.865 \pm 0.136$  Sv has been recently obtained by García-Lafuente et al. (2021) from the analysis of experimental data recorded over the period 2004–2012. The averaged simulated Atlantic inflow is 0.93 Sv, which is also in the range of published values (e.g. 0.78 Sv in Tsimplis and Bryden 2000; 0.96 Sv in García-Lafuente et al. 2002). The net transport for the historical experiment is in excellent agreement with the hindcast value, although exhibiting reduced variability, yet it results from higher inflow and outflow.

The net transport across both Turkish Straits (TSS) is on average negative, consistently with the observed net inflow of fresher waters into the Aegean Sea from the Black Sea, where precipitation and river discharge exceed evaporation. The magnitude of the inflow appears to be lower than previous observational and numerical estimates, which range from 0.006 Sv to 0.01 Sv (Ünlüata et al., 1990; Simonov and Altman, 1991; Peneva et al., 2001; Kara et al., 2008; Sannino et al., 2017).

However, fluxes through the TSS are difficult to accurately measure, due to the large variability in the observed currents and the consequent low signal-to-noise ratio, which might need longer-term monitoring to be adequately increased (Sannino et al., 2017). On the other hand, the simulated net transport is expected to significantly benefit by further refining the grid in correspondence of both Straits, as demonstrated by Sannino et al. (2017), where a very-high-resolution simulation was performed to accurately reproduce transports with the prescription of climatological barotropic forcing at the two open boundaries. Increased resolution together with a specific treatment of local viscosity and diffusivity is therefore liable to enhance water exchanges across the straits, and to further improve the already good model performance.

## 3.2 Basin hydrology and circulation

We first compare model climatologies of the winter and summer sea surface temperature (SST) and SSS with reanalysis data; mean fields are computed over the common period 1987–2005. In Fig. 2, panels (a-b) are for the Mediterranean Optimally Interpolated Sea Surface Temperature (OISST) reanalysis of Marullo et al. (2007), panels (c-d) for the Copernicus reanalysis, panels (e-f) for the hindcast, and panels (g-h) for the historical simulation. The model simulations are in an overall good agreement with the reanalyses, even though MED16 systematically produces lower temperatures in winter (more so in the historical simulation). In summer, the SST from the hindcast is in excellent agreement with both reference fields, whereas the historical simulation displays slightly warmer temperatures in the western basin, in the central part of the eastern basin and in the Adriatic Sea, and lower ones in the Ionian, and in the easternmost part of the Levantine.

In Fig. 3, the SSS model climatologies (panels c-d, hindcast; panels e-f, historical), are compared with the Copernicus reanalysis (panels a-b). In the western basin, the hindcast salinity appears to slightly overestimate the observations in both seasons, although less notably so in summer. In the eastern basin, the salinity field is generally well reproduced in winter, while in summer some local negative biases are present (e.g. in the Gulf of

Gabes, in the Adriatic Sea, and in the north Aegean). The historical experiment, on the contrary, exhibits larger salinity values in both seasons and basins, yet reducing the positive bias around the Balearic Islands, coherently with the limited intrusion of the Atlantic Water (AW) into the Tyrrhenian Sea, the Sicily channel and the Gulf of Gabes, and with the more pronounced northward spreading of the Atlantic inflow after exiting the Alboran Sea.

Specific local differences between the numerical experiments and the reanalysis can be attributed to the different treatment of rivers and/or to the different magnitudes of the runoff provided by the driving atmospheric simulations (e.g. along the eastern Adriatic coast and in the North Adriatic Sea), while the different behaviour of the two MED16 runs in the North Aegean is probably related to the representation of the local circulation, as no significant difference was detected in the representation of the net inflow from the Dardanelles between the hindcast and the historical experiment. This discrepancy will be the object of future research.

The hydrological structure and the circulation produced by the hindcast and historical simulations were further validated via comparison with in situ and remote observations. Vertical means of the modelled and reanalysed temperature and salinity were computed over the 1987–2005 time window, for three different vertical layers, and averaged over the whole Mediterranean basin (MED), and the western and eastern sub-basins (WMED and EMED). Table 2 shows the reference values from the reanalysis, together with the differences between model and reference for the two experiments, for the surface layer (0 -150m), the intermediate layer (150-600m), and the deep layer (600-3500m).

Table 2

For each geographical area in the leftmost column - the whole Mediterranean (MED) and the Western (WMED) and Eastern (EMED) sub-basins - the first row reports the average temperature ( $^{\circ}\text{C}$ ) and salinity ( $\text{Psu}$ ) at various depths, from the Copernicus Reanalysis dataset; the second and third rows (labelled "*hindcast*" and "*historical*") respectively report the associated differences between the hindcast and the historical simulations and the reanalyses. All spatial averages are taken over the period 1987–2005

		Temperature			Salinity		
		Depth [m]			Depth [m]		
		0-150	150-600	600-3500	0-150	150-600	600-3500
<b>MED</b>	Reanalysis	16,54	14,00	13,32	38,39	38,81	38,65
	Hindcast	-0,64	-0,14	0,05	-0,12	-0,15	-0,04
	Historical	-0,78	-0,27	0,18	0,04	-0,08	0,04
<b>WMED</b>	Reanalysis	15,37	13,45	12,93	37,83	38,49	38,47
	Hindcast	-0,39	-0,29	0,01	-0,04	-0,10	0,01
	Historical	-0,57	-0,38	0,09	0,01	-0,05	0,07
<b>EMED</b>	Reanalysis	17,17	14,34	13,55	38,70	38,84	38,80
	Hindcast	-0,74	-0,06	0,08	-0,15	-0,03	0,00
	Historical	-0,86	-0,21	0,26	0,07	0,05	0,09

Despite the differences highlighted in the spatial patterns, the agreement between the hindcast and historical simulation and the reference data is good. However, the modelled temperatures are always slightly lower than the observations in the two upper layers and slightly higher in the deep layer. For both simulations and all geographical areas, maximum discrepancies are anyway found in the surface layer, with largest differences in the Eastern basin. When the whole basin is considered, modelled salinity also generally presents negative anomalies, with maximum negative differences in the surface and intermediate layers of the hindcast simulation, while slightly positive anomalies can be observed in the surface and bottom layers for the historical simulation. When separately considering the two sub-basins, the hindcast experiment exhibits more marked negative biases in the intermediate layer of the Western basin and in the surface layer of the Eastern basin, while the historical simulation projects higher salinity in the surface layer of the Eastern basin with respect to the reanalysis. We note that the biases for temperature and salinity are well inside the ensemble spread computed by Llasses et al. (2018) from the Med-Cordex simulations.

In order to evaluate the ability of the hindcast experiment in reproducing the time evolution of water temperature, Fig. 4 shows the time series (1987–2010) of the mean annual temperature anomalies in the surface and intermediate layers, for the whole basin and the western and eastern sub-basins, as simulated by the hindcast experiment. Comparison with the historical simulation is omitted here as time coherence with the reanalysis could not be expected. The observed interannual variability is generally well captured by the hindcast simulation, both in the surface and in the intermediate layer.

The simulation correctly reproduces the observed interannual variability. The EMED time series, in particular, captures the positive trend in both the upper and intermediate layers. Moreover, the simulation well represents the strong cooling during the years 1992 and 1993, that is the signature of the Eastern Mediterranean Transient (EMT) phenomenon.

Analogous considerations apply to the time series of mean annual salinity anomalies (Fig. 5). The general trend of simulated salinity and reanalysis are also similar, except for the intermediate layer of WMED where the simulated salinity does not follow the reanalysis trend. In the WMED the model captures both the sudden drop in salinity around 1990 and the maximum in 2005. The first event is due to an excess of freshwater input and is confined to the upper layers, whereas the latter is related to a well-known event of intense dense water formation in the Gulf of Lion. A good representation of the interannual variability of the salinity field is also achieved in the EMED, with a local maximum during the 90s and an increasing trend in the second half of the simulation.

A notable discrepancy occurs in the years from 2001 to 2004, in which the reanalysis displays a relative minimum, particularly strong in the WMED, which is not present in the model. However, the corresponding data from the MEDHYMAP dataset show a very good agreement with MED16 also for the period 2000–2005.

Figure 6 shows the surface (15 m of depth) and intermediate (300 m of depth) model circulations, averaged over the simulation time-span (1982–2010).

At both depths, the model circulation is close to the 1987–2007 time-mean flow displayed in Pinardi et al. (2015), which results from a reanalysis of the Mediterranean Sea circulation (see their Figs. 3 and 4, displaying the circulation at 15 m of depth, and the average circulation in the layer from 200 m and 300 m of depth). The main Mediterranean surface current systems, either driven by the local wind forcing, or by the inflow of AW at the Gibraltar Strait, are present both in our hindcast and in the reanalysis, with similar shapes. This also applies to most of the robust cyclonic and anticyclonic circulation structures, even though there are a few features, such as the quasi-permanent cyclonic circulation to the southeast of Sardinia, and some smaller vortices in the eastern basin, that are not well defined in the hindcast. Overall, considering that the latter is the result of a “free” simulation spanning almost three decades, whereas the reanalysis relies on the assimilation of observed data, the representation of the average Mediterranean circulation provided by our model can be considered quite satisfactory.

Three hindcast sub-regional surface circulation maps are displayed in Fig. 7. Panel (a) of the figure highlights the two permanent cyclonic circulations that characterize the northern portion of the western Mediterranean, that is, the wide gyre formed by the Liguro-Provençal current, occupying the western Ligurian Sea, and the Bonifacio cyclone, in the northern part of the Tyrrhenian Sea, to the east of Corsica. Interestingly, between the two cyclonic circulations, there is the weak signature of an anticyclonic circulation, in the area of the Corsica Channel, between Cap Corse (the long peninsula in the northern tip of Corsica) and the Italian coast. This structure, which was denoted as Ligurian anticyclone in Ciuffardi et al. (2016), appears to be a robust feature of the local dynamics during the summer months (see also recent works by Poulain et al., 2020, and by Iacono and Napolitano, 2020).

As shown in Fig. 7b, the model correctly reproduces the wide cyclonic structure, with two poles, that occupies the southern, deeper portion of the Adriatic Sea (see, e.g., recent work by Palma et al., 2020, and references therein).

Finally, we note that the surface dynamics of the Marmara Sea (Fig. 7c) are dominated by a central, elongated gyre, more attached to the northern coast, in agreement with what was found in a recent high-resolution numerical investigation of the Turkish Straits System by Sannino et al. (2017).

The time evolution of the Mixed Layer Depth (MLD - Fig. 8) highlights how deep-water-formation processes in the Gulf of Lion and the Adriatic basin are well represented both in the hindcast and in the historical experiments.

## 4. Hindcast And Historical Sea-level Analysis

The Mediterranean Sea level average and variability simulated in the hindcast experiment are compared to their observed counterparts, derived from altimetric satellite sea level anomaly (SLA) measurements. The model ability to reproduce nearshore sea level is assessed by means of tide gauge data.

### 4.1 Comparison with satellite observations

The altimeter data used are daily maps of gridded L4 SLA and derived variables reprocessed (Copernicus portal, <http://marine.copernicus.eu>, last access april 2021), obtained from the merging of track data from different satellites. These maps, especially developed for the Mediterranean Sea, have a nominal resolution of  $1/8^\circ \times 1/8^\circ$ , which is twice the resolution of the products that cover the world ocean. They have been available since 1993, overlapping the last 18 years of the simulation. A different altimeter dataset was used in Adloff et al. (2018) (see Ablain et al., 2015, for details), which consists of monthly SLA maps with a spatial resolution of  $1/4^\circ$ .

The average seasonal cycle reproduced by the hindcast is compared to that of the observations in Fig. 9, where the solid lines with black dots refer to model results and the dashed lines with diamonds to altimeter data (the averages are over the period 1993–2010). Panel (a) shows that the model cycle over the whole basin is fairly close to the observations, with some overestimation in winter and some underestimation at the end of summer and in part of the autumn.

Overall, the model cycle is close to that obtained from the NEMO-MED12 simulation discussed in Adloff et al. (2018), which was found to provide the best SL reconstruction among the four considered in that work.

The two other panels in the figure show the same comparison for the western and eastern sub-basins, respectively. The cycle for the western Mediterranean is even closer to the observations than the basin cycle, whereas in the eastern basin, where the amplitude of the observed cycle is slightly larger, the model underestimation during SON is also larger. This may be due to the fact that the steric contribution to the SL, which is in principle absent in most state-of-the art circulation models, is here introduced indirectly through the Atlantic boundary conditions. As we have seen, this works pretty well, particularly in the western basin, but it

may be not sufficient to account for additional sea-level seasonal variations induced by local heat fluxes, especially in the eastern sub-basin.

The interannual variability of the sea-level anomaly of the hindcast simulation is shown in Fig. 10, where the same notations of the previous figure are adopted. The plotted values are yearly anomalies with respect to the mean over the period covered by the altimeter (1993–2010), averaged over four different regions: the Atlantic box, the whole Mediterranean basin, the WMED, and the Levantine sub-basin. The first panel is relative to the Atlantic box, i.e., the small domain to the west of the Gibraltar Strait where boundary conditions are prescribed, making use of the available altimetric data (see Sect. 2 for details). From 1993 on, the model time series appears well correlated with the observations, showing that the boundary conditions are correctly applied in our model. In fact, the cross-correlation coefficients of Table 3 show that the model time series are very well correlated with the corresponding altimeter-derived time series in all the basins in consideration.

Table 3  
Cross-correlation between the yearly sea level anomaly time series and that of the SLA, over the period 1993–2010, for four different basins

	<b>Atlantic box</b>	<b>Mediterranean</b>	<b>Western Med.</b>	<b>Levantine</b>
Correlation with SLA	0.81	0.81	0.78	0.87

The time series of the average Mediterranean SL anomaly (top right panel in Fig. 10) reproduces the growing basin-scale trend displayed by the altimetric observations (see Bonaduce et al., 2016, and the more recent investigation by Mohamed et al., 2019, where trends of the SL in the Mediterranean were discussed, based on 25 years of altimeter data). It also captures short-time variations, such as the sharp increase seen in 2010, which results from a large wintertime jump of the SL over the whole Mediterranean Sea. As shown in Landerer and Volkov (2013), this was due to a basin-wide barotropic fluctuation induced by the variation of the wind stress in the Gibraltar area and in the neighboring Atlantic sector, associated with inflow of Atlantic water through the Gibraltar Strait. A similar event occurred during the following winter of 2011.

Comparison with Fig. 4 of Adloff et al. (2018) shows that the model time series of Mediterranean anomalies also captures the main interannual variability observed before 1993; the reference for this period is provided by two reconstructions of the Mediterranean SL by Calafat and Jordà (2011), and Meyssignac et al. (2011), based on data from coastal tide gauges. The series is also in good agreement with that obtained from the NEMO-MED12 simulation of Adloff et al. (2018). This is due to the fact that, despite the many differences, the two models apply the same Atlantic boundary conditions, and use as local atmospheric forcing two different downscaling of the same dataset (ERA-INTERIM). In some cases, the model series displays stronger SL variations; this may be ascribed to model differences, but could also partly be due to the contribution of mesoscale features that are better resolved by the model, thanks to the higher horizontal resolution ( $1/16^\circ$ ). This holds a fortiori, when compared with the altimeter data, whose nominal resolution is  $1/8^\circ \times 1/8^\circ$ .

The lower row of Fig. 10 shows the SL anomalies for the sub-basin that is closest to the Atlantic (western Mediterranean) and for that more far away from it (Levantine basin, to the east of  $22^\circ$  of longitude). The signals are quite different in the two sub-basins; the series in the western Mediterranean resembles that in the Atlantic box, with a fairly regular increase of the SL over the simulation period, whereas that in the Levantine

shows a decrease of the SL at the end of the 80's and beginning of the 90's, followed by a sharp increase, leading to a different state over the last 10 years of the simulation. The latter behavior is of course related to the Eastern Mediterranean Transient (EMT), the major event that has affected the circulation and water mass properties of the Mediterranean in the last decades. The hindcast is capable of reproducing the rapid SL rise as a result of strong anomalous mass modification in the deep layers of the EMED during the end of the 80s and the beginning of the 90s; the effects of the EMT on sea level has been discussed for the first time by Tsimplis and Josey (2001). The model correlates very well with the altimeter observations after the transient, which display a definitely nonlinear trend, first evidenced in Amitai et al. (2010).

We can conclude that the hindcast simulation not only captures the basin scale variability of the SL over the hindcast period, but also some expected, significant differences between the main Mediterranean sub-basins.

In Fig. 11, the modelled (both hindcast and historical) SSH fields, averaged over the period 1993–2011, are compared with the corresponding climatological average of the absolute dynamic topography (ADT) from altimeter data (AVISO, <http://www.aviso.oceanobs.com>, last access May 10th 2021). In all cases, the respective regional climatological means have been subtracted to ease the comparison of patterns. Being a long-term average, the field derived from the AVISO data is expected to be very close to the Mean Dynamic Topography (MDT), that is, to the mean signal, representative of the average circulation, which produces the ADT when added to the zero-mean remotely measured sea level anomaly (SLA). The reference observational field shown in Fig. 11 is indeed very close to that of Rio et al. (2014), which was constructed using observations and model results, and validated using independent observations.

The spatial pattern of the modelled SSH field generally appears to be in good agreement with the observations, and is also similar to that obtained by the NEMO-MED12 model, the best performing among those considered in Adloff et al. (2018). As to the hindcast experiment, the MED16 model outperforms NEMO-MED12 in the western portion of the basin, indicating that the stretched grid at Gibraltar indeed allows for a better representation of the complex dynamics inside the Strait. Nevertheless, the signatures of the Rhodes gyre and of the western Cretan gyre are weaker than expected. On the other hand, neither the MED16 simulation nor the four hindcasts analyzed in Adloff et al. (2018) resolve the Ierapetra gyre, possibly due to the still insufficient spatial resolution or to the quality of the downscaled wind forcing in the area, the Ierapetra gyre being a wind driven feature.

The SSH values obtained for the Black Sea (not shown here) exhibit larger spatial variability with respect to those of the Mediterranean Sea, approximately ranging from – 6 cm to 18 cm, and compare well with the MDT reconstructions by Knysh et al. (2002) and by Kubryakov and Stanichny (2011). In particular, Kubryakov and Stanichny (2011) find localized, deeper minima in the core of the dominant cyclonic cell, while MED16 produces significantly higher SSH values than either reconstruction in the westernmost portion of the same cell.

## 4.2 Comparison with tide gauges

Hindcast sea surface heights along the coast have been compared with tide gauge data retrieved from the Permanent Service for Mean Sea Level (PSMSL) (Holgate et al., 2013; PSMSL, 2020).

In particular, we used time series of sea level monthly means from the Revised Local Reference dataset (RLR), which are independently calibrated for each station in the PSMSL according to the tide gauge history provided by each local supplying authority. However, no correction is made by PSMSL for vertical land movements (VLM), although tide gauges without known benchmarks are omitted from this data set by PSMSL prior to release (Hamlington et al., 2016). These data therefore measure the relative movement of the sea surface with respect to the land, disregarding the multiple processes over a variety of time scales that can affect MSL estimates, some of natural origin, such as the glacial isostatic adjustment (GIA) and plate tectonics, and some related to human activities (e.g. ground-water pumping). In the following, RLR data have been used without any further correction for VLM, selecting all the available Mediterranean stations which covered at least 50% of the simulated period. In order to avoid relative biases due to different zero-level assumptions, monthly data from the model grid point nearest to the tide gauge have been compared with the monthly mean tide gauge data after subtraction of the respective mean values, over the common time interval, from both modelled and tide gauge time series.

The 34 locations for which the comparison was carried out are shown in Fig. 12.

The cross-correlation coefficients obtained are detailed in Table 4, where the geographic location of the stations and the number of observations are also indicated.

The coefficients are pretty high in most of the stations; they are smaller than 0.65 only in 8 stations (17, 23, 25, 26, 28, 29, 31, 34) located in the Aegean Sea or nearby, and one in the Black Sea. This is quite encouraging, considering that the model values are not at the stations' sites, which are very close to the coast, and that the model freely evolves for three decades. It shows that, in part of the basin, the model is capable of providing a fairly accurate description of the sea level variability on long time scales, not only over large spatial scales, but also nearshore, where the consequences of sea level change are stronger. The fact that the model performs less well in the Aegean Sea is likely partly due to difficulties in reproducing small scale details of the near coast dynamics, induced by the very complex bathymetry of the area.

Table 4

List of tide gauges used with the corresponding code number and coordinates. Correlation between the observed time series and model data is shown together with the standard deviation of the two series of data and the number of times considered

number	station	code	longitude	latitude	correlation	n. times	std station	std model
1	TARIFA	488	-5,616	36,020	0,651	321	6,821	4,177
2	ALGECIRAS	490	-5,422	36,132	0,717	249	5,974	3,936
3	CEUTA	498	-5,299	35,910	0,659	330	5,502	4,205
4	MALAGA	496	-4,407	36,668	0,777	349	7,606	4,469
5	PORT VENDRES	1469	3,094	42,594	0,766	210	7,952	6,113
6	L'ESTARTIT	1764	3,281	42,031	0,825	241	7,472	6,630
7	MARSEILLE	61	5,344	43,281	0,797	316	7,207	6,318
8	TOULON	980	5,906	42,969	0,711	217	7,041	6,772
9	NICE	1468	7,281	43,656	0,717	300	7,101	6,373
10	VENEZIA (PUNTA DELLA SALUTE)	168	12,406	45,281	0,813	239	8,804	8,607
11	ROVINJ	761	13,656	45,094	0,799	349	8,246	8,630
12	TRIESTE	154	13,781	45,656	0,810	349	8,450	8,718
13	SPLIT - GRADSKA LUKA	352	16,406	43,344	0,761	349	7,925	8,293
14	SUCURAJ	1706	16,906	43,031	0,732	221	8,431	8,321
15	DUBROVNIK	760	18,031	42,656	0,754	345	7,568	8,049
16	LEVKAS	1239	20,719	38,906	0,702	310	9,384	7,356
17	PREVEZA	410	20,719	38,906	0,585	301	7,579	7,380
18	KATAKOLON	1240	21,344	37,656	0,717	300	7,720	7,412
19	KALAMAI	411	22,156	36,969	0,770	276	7,947	7,677
20	THESSALONIKI	373	22,844	40,536	0,680	329	8,847	8,014
21	NORTH SALAMINOS	1604	23,531	37,906	0,735	180	8,305	7,856
22	SOUDHAS	1232	24,094	35,781	0,678	338	7,668	7,607
23	SIROS	1234	24,969	37,531	0,577	317	8,687	7,644
24	IRAKLION	634	25,156	35,531	0,669	235	10,500	7,208
25	ALEXANDROUPOLIS	1238	25,906	40,825	0,635	312	8,132	7,820
26	KHIOS	408	26,156	38,656	0,622	316	8,108	7,746

number	station	code	longitude	latitude	correlation	n. times	std station	std model
27	MENTES/IZMIR	1679	26,719	38,594	0,686	265	8,062	7,785
28	LEROS	1233	26,844	37,094	0,522	300	6,432	6,800
29	RHODOS	1243	28,219	36,469	0,649	220	7,741	6,415
30	ALEXANDRIA	503	29,906	31,281	0,708	301	9,142	7,470
31	ERDEK	1598	27,856	40,383	0,478	255	9,030	6,460
32	ANTALYA II	1681	30,719	36,781	0,736	253	9,541	7,811
33	TUAPSE	215	39,125	44,026	0,724	346	9,428	9,200
34	POTI	41	41,622	42,192	0,533	336	12,538	9,128

Sea surface height time series for six stations (red circles in Fig. 12) where VLM can be considered to be negligible are plotted in Fig. 13. The main interannual variability is reproduced fairly well at all stations, and especially at Malaga, Trieste, Preveza and Alexandria.

## 5. Scenario Simulation

### 5.1 Future basin hydrology and circulation

For the RCP8.5 scenario, Fig. 14 shows the differences in the future surface temperature climatologies with respect to the reference period. Averages are computed over years 2046–2065 (left) and 2081–2100 (right), for winter (top) and summer (bottom). The sustained increase in temperature is evident in both seasons. As for the correspondent salinity fields (Fig. 15), the salinification of the Eastern basin is apparent, especially in the north, as well as the northward displacement of the Atlantic stream in the Western basin, yet accompanied by a more efficient penetration of the AW into the Ionian basin under the future scenario with respect to the historical simulation.

The temperature-induced additional buoyancy is evident in the mixed layer depth which exhibits significantly lower relative maxima at dense water formation sites. The deep convection in the Gulf of Lion is almost neutralised, whereas in the Adriatic Sea is characterised by enhanced variability (Fig. 16).

Basin-wide averages of T and S are summarized in Table 5, where substantial increases in temperature generally characterize the surface and intermediate layers, while variations in salinity appear to be most relevant and coherent in the intermediate layer. Results are consistent with the findings of Soto-Navarro et al. (2020).

Table 5

Average temperature ( $^{\circ}\text{C}$ ) and salinity ( $\text{Psu}$ ) at different depths. Differences between values averaged over two periods (2046–2065 and 2081–2100) of the scenario simulation and the whole period (1981–2005) of the historical simulation. Averages are over the whole Mediterranean Sea (MED), and over the western and eastern sub-basins (WMED and EMED)

		Temperature			Salinity		
		Depth [m]			Depth [m]		
		0-150	150-600	600-3500	0-150	150-600	600-3500
MED	RCP 2046–2065	1,72	1,48	0,25	-0,03	0,22	0,00
	RCP 2081–2100	3,31	2,76	0,56	0,20	0,44	0,06
WMED	RCP 2046–2065	1,46	1,44	0,45	-0,10	0,27	0,07
	RCP 2081–2100	2,98	2,76	0,83	-0,01	0,47	0,15
EMED	RCP 2046–2065	1,87	1,49	0,11	0,02	0,20	-0,03
	RCP 2081–2100	3,50	2,76	0,36	0,32	0,42	0,02

## 5.2 Impact of dynamical downscaling on the projected SLC

Figure 17 separately quantifies the magnitude and sign of the components, either local or global, that contribute to a projected mean sea level trend of about 7 mm/yr in the Mediterranean, and allows the evaluation of their relative weight. Under RCP8.5 and from 2005 to 2100, it shows the time evolution of each respective central estimate, the ocean dynamic component being derived from an ensemble of 16 GCM participating in the CMIP5 programme, after excluding simulations that do not explicitly represent the open connection between the Mediterranean Sea and the Atlantic Ocean (<https://icdc.cen.uni-hamburg.de/en/ar5-slr.html>, Slangen et al., 2014).

Prior to spatial averaging, all the variables have been interpolated onto the MED16 grid via a bilinear interpolation, with nearest-neighbor interpolation near the coasts, results from the MED16 regional projection are also shown. The zero level is set at the 1986–2005 mean that Slangen et al. (2014) consider as the common zero SSH anomaly value.

The most relevant contribution is that from the stericodynamic term (dark red; solid line = GCM, dashed line = MED16), which accounts for changes in the circulation and density distribution of sea water and for the inverse barometer (IB) correction associated with atmospheric pressure patterns (Gregory et al., 2019). Positive changes (here listed in decreasing order) also derive from distributed glacier melting (aside from Greenland and Antarctica ice sheets - green), Antarctic dynamic ice loss (pink), Greenland surface mass balance (light blue), Greenland dynamic ice loss (blue) and glacial isostatic adjustment (red), ground water storage (yellow), while the Antarctic surface mass balance (dark green) determines a reduction in sea level. At the end of the XXI century, these components are projected to respectively account for 51%, 23%, 13%, 10%, 6%, 2.5%, 2%, -7% of the total, with an overall contribution of 16% from Greenland and 6% from Antarctica. Recent works (Spada, 2017; Santamaría-Gómez et al., 2017) have dwelled on the necessity to consistently include the GIA effect in updated estimates of SLC in the Mediterranean, based on the alternative datasets provided by Lambeck

(Lambeck et al., 1998) and Peltier (Peltier et al., 2004), whose limits and reliability have been the subject of a lively scientific discussion (Peltier, 2002; Lambeck et al., 2002). Here, the GIA contribution is the one computed by Church et al. (2013b) by averaging results from the ICE-5G model (Peltier et al., 2004) and the ANU ice sheet model (Lambeck et al. 1998 and subsequent improvements), using the updated SELEN code for the sea level equation (Spada and Stocchi 2006, 2007). In the Mediterranean basin, however, despite its comparative importance for the assessment of relative sea level rise for present times, the GIA contribution appears to progressively lose relevance by the end of the XXI century, unless ongoing research revises the long-term ranking of individual contributions.

Although only representing one of the numerous possible realizations that can be obtained by different GCM-RCM modelling chains, the MSL trend estimated via the MED16 scenario simulation is very similar to that of the GCM ensemble mean from Slangen et al. (2014), although it slightly accelerates from 2040 onwards. With respect to the coarse-resolution global average, the MED16 downscaling better characterizes the regional patterns of SLC arising from ocean dynamics, and it consequently retains enhanced variability.

The time evolution of the difference in SSH between the Mediterranean basin interior and the neighbouring Atlantic Ocean (average over the region just outside the Gibraltar Strait, from 9W to 6W) is reported in Fig. 19, for both the MED16 model (left panel) and the global ensemble mean (right panel). The red curves correspond to the stericodynamic term (i.e., to the dark red curves of Fig. 17), the yellow curve in the left panel represents the historical reference experiment, while the AVISO observations are plotted in black. Beside the good agreement between the AVISO data and the historical experiment, it is worth noting that the regional simulation is capable of capturing the hydraulic jump across the Gibraltar Strait (Fig. 18) that is completely missed by the global projection, due to the insufficient representation of the local dynamics (Sannino et al. 2009, 2015). Nevertheless, the global experiment also exhibits the relative “sinking” of the Mediterranean with respect to the Atlantic, albeit following a trend that is half that of the regional experiment, and characterized by lower variability. Some coherence is yet detectable between the respective typical time-scales of variability, possibly when driven by large-scale patterns, as well as a comparable signal-to-noise ratio. However, the global projection seems to be reaching a new stable state towards the end of the XXI century that is not discernible in the regional experiment, a longer run being needed to confirm such a hypothesis. So far, the change in the relative level between the two basins can be estimated to be within centimeters, over an expected sea level increase on the order of tens of centimetres by the end of the century.

Figure 20 illustrates the spatial distribution of the progressive increase in sea level under RCP8.5 with respect to the historical period 1985–2005, which qualitatively retains the overall pattern of the dynamic topography under current climate, where the largest increments apparently correspond to the Atlantic signal, mirroring the AW progress into the basin interior. The main notable difference appears to be the sustained amplified signal around the Balearic Islands, presumably itself a consequence of the northward displacement of the Atlantic inflow that numerical models associate with the newly detected Western Mid-Mediterranean Current (WMMC). This current corresponds to the northward meandering stream arising from the bifurcation of the Atlantic inflow after exiting the Alboran Sea and overcoming the Almera-Oran front (Arnone et al., 1990, Pinardi et al., 2015). The WMMC branch of the Atlantic inflow has also been detected in the hindcast and historical experiments (Fig. 6), yet it has never been well documented in observational datasets. Pinardi et al. (2015) tentatively interpret it as a residual current resulting from multi-year averaging.

Figure 21 reports the differences between MED16 and the GCM ensemble mean for the two targeted time horizons. The overall pattern is maintained in time, with localized yet roughly constant negative biases (i.e., CGM estimates are higher) in the Levantine basin, and positive biases in the Ionian Sea and the Western basin, generally not exceeding 10÷12 cm, and an increasingly more pessimistic regional projection for the Balearic region, going from a deviation of 15÷17cm at mid-century, to one of 17÷22 cm in 2100.

## 6. Conclusions

We have here analysed the results of three climatic simulations of the Mediterranean Sea circulation and sea level, performed with MED16, an updated version of the tide-including, climatic ocean model presented in Sannino et al., (2015). These consist of a hindcast simulation, covering three recent decades (1981–2010), a historical run (1981–2005), and a future climate simulation, under the RCP8.5 scenario, which starts from the end of the historical run and proceeds until the end of the present century (2006–2100).

The hindcast simulation has been used to assess the ability of the new model to reproduce the past evolution of the basin circulation, with excellent results. This simulation has a value in itself, because it is the first pluri-decadal, eddy-resolving simulation of the Mediterranean Sea circulation that includes the main tidal effects, together with an accurate treatment of the complex dynamics occurring in the Gibraltar Strait area. We have therefore preliminarily analysed the simulated transports at the Gibraltar, Dardanelles and Bosphorus straits, and the basin hydrology and circulation. We found that the model correctly represents the transport evolution at Gibraltar, the average circulation in the surface and intermediate layers, and the main variability of the Mediterranean hydrologic structure during the simulation period. The simulated SLA was found in good agreement with satellite observations, exhibiting a positive trend in the Western Mediterranean Sea, and a more complex behavior in the Levantine basin, where sea level variability has been strongly influenced by the EMT and its evolution.

The spatial structure of the hindcast average SSH field is well reproduced over the entire basin, especially in the western Mediterranean where results are much closer to that of the MDT, due to the fact that the use of improved sea level information at the Atlantic lateral boundary significantly enhances the reliability of results. A further improvement has been obtained through the adequate treatment of the complex, hydraulically driven dynamics across the Gibraltar Strait. The evolution of the hindcast SSH near coast compares very well with tide gauge observation along most of the basin's coasts. This shows that MED16, if adequately forced, can provide useful information on the sea level variability in coastal areas, which are the more exposed to SLR, even though the current horizontal resolution of the model does not allow to exactly resolve the locations of the tide gauge stations. This also provides an indirect check of the general quality of the atmospheric forcing from the SMHI downscaling. This suggests that further improvement of the forcing may be needed to obtain an even more realistic description of the circulation structure.

The historical simulation, which sets the reference baseline for the future scenario projections, also correctly reproduces the main mean features of the Mediterranean circulation and hydrology, a result that is all the more satisfactory when considering that no specific constraint or relaxation is prescribed.

Under the RCP8.5 future scenario, the temperature is projected to generally increase. The spatial pattern of variations in surface salinity is affected by the penetration of the Atlantic stream into the basin interior, with

the westernmost regions exhibiting appreciable decreases. The warming of sea waters results in the inhibition or enhanced convection variability in the main deep-water formation sites.

As regards future sea level, the overall DSL trend estimated by MED16 is comparable to the ensemble mean computed from the Global Circulation Models analysed in Slangen et al. (2014). Nevertheless, our regional dynamical downscaling provides a better characterization of regional patterns arising from ocean dynamics and of their variability, and gives a more pronounced relative sinking of the Mediterranean with respect to the Atlantic. The regional differences in SLR between the presented downscaling and the GCM mean projection are generally constant in time, yet an acceleration emerges in the regional projection for the Balearic area.

Indeed, state-of-the-art numerical estimates show that future sea level rise in the Mediterranean basin will crucially depend on the evolution of the steric component, as determined by the propagation of the Atlantic signal through the Strait of Gibraltar and by the local circulation. MED16 effectively provides an accurate and reliable representation of the basin's DSL, by accounting for the numerous and complex processes that concur to determine it. Nevertheless, in view of the significant numerical resources it demands, the assessment is recommended of the minimum requirements MED16, or any other similar model, must comply with, in terms of resolution and explicit process representation. In accordance with previous works, we demonstrate that both explicit tidal forcing and an accurate resolution of the Gibraltar Strait are key features that cannot be disregarded in designing numerical tools suitable for the DSL simulation in the Mediterranean Sea.

## Declarations

### Author Contributions

Conceived the work [GS]

Implemented the model and performed the run [GS, AC]

Collected data [MP, EN, RI, AC]

Designed the analysis [GS, RI, AC, EN, GP, MVS]

Performed the analysis [RI, AC, MP, EN]

Wrote the paper [ALL]

### Acknowledgements

Regional sea level data from IPCC AR5 distributed in netCDF format by the Integrated Climate Data Center (ICDC, icdc.cen.uni-hamburg.de) University of Hamburg, Hamburg, Germany. SROCC sea-level rise data are available at <https://www.ipcc.ch/srocc/download-report/>.

## References

1. Ablain M, Cazenave A, Larnicol G, Balmaseda M, Cipollini P, Faugère Y, Fernandes MJ, Henry O, Johannessen JA, Knudsen P, Andersen O, Legeais J, Meyssignac B, Picot N, Roca M, Rudenko S, Scharffenberg MG, Stammer D, Timms G, and Benveniste J (2015) Improved sea level record over the satellite altimetry era (1993–2010) from the Climate Change Initiative project. *Ocean Sci.* 11:67–82. <https://doi.org/10.5194/os-11-67-2015>, 2015.
2. Adcroft A, Campin JM (2004) Rescaled height coordinates for accurate representation of free-surface flows in ocean circulation models. *Ocean Model* 7(34):269–284
3. Adloff F, Jordà G, Somot S, Sevault F, Arsouze T, Meyssignac B, Li L, and Planton S (2018) Improving sea level simulation in Mediterranean regional climate models. *Clim Dyn*, 51:1167–1178
4. Amitai Y, Lehahn Y, Lazar A, Heifetz E (2010) Surface circulation of the eastern Mediterranean Levantine basin: Insights from analyzing 14 years of satellite altimetry data. *J. Geophys. Res.* 115, C10058.
5. Antonioli F et al (2017) Sea-level rise and potential drowning of the Italian coastal plains. Flooding risk scenarios for 2100. *Quaternary Science Review* 158:29–43, doi: 10.1016/j.quascirev.2016.12.021.
6. Arnone RA, Wiesenburg DA, Saunders KD (1990) The origin and characteristics of the algerian current. *Journal of Geophysical Research* 95 (C2):1587–1598. <http://dx.doi.org/10.1029/JC095iC02p01587>.
7. Balmaseda MA, Mogensen K, Weaver AT (2013) Evaluation of the ECMWF ocean reanalysis system oras4. *QJR Meteorol Soc* 139(674):1132–1161.
8. Bignami F, Marullo S, Santoleri R, and Schiano ME (1995) Longwave radiation budget in the Mediterranean Sea. *J. Geophys. Res* 100:2501–2514.
9. Bonaduce A, Pinardi N, Oddo P, Spada G, and Larnicol G (2016) Sea-level variability in the Mediterranean Sea from altimetry and tide gauges. *Climate Dynamics* 47(9–10): 2851–2866.
10. Bougeault P, and Lacarrère P (1989) Parameterization of Orography-Induced Turbulence in a Mesobeta-Scale Model. *Monthly Weather Review* 117:1872-1890. [http://dx.doi.org/10.1175/1520-0493\(1989\)117](http://dx.doi.org/10.1175/1520-0493(1989)117)
11. Boutov D, Peliz A, Miranda PMA, Soares PMM, Cardoso RM (2014) Inter-annual variability and long term predictability of exchanges through the Strait of Gibraltar. *Glob Planet Change* 114:23–37. doi:10.1016/j.gloplacha.2013.12.009
12. Calafat FM, Jordà G (2011) A mediterranean sea level reconstruction (1950–2008) with error budget estimates. *Glob. Planet. Change* 79:118–133.
13. Campin JM, Adcroft A, Hill C, Marshall J (2004) Conservation of prop- erties in a free-surface model. *Ocean Model* 6:221–244.
14. Candela J (2001) Mediterranean water and global circulation. In: Siedler G, Church J, Gould J (eds) *Ocean circulation and climate*. Academic, San Diego, pp 419–429
15. Church JA, Clark PU, Cazenave A, Gregory J, et al (2013a) Sea level change, in *Climate Change 2013: The Physical Science Basis*. Stocker TF, Qin D, Plattner GK, et al (ed) Cambridge University Press, Cambridge, UK and New York, NY. USA.
16. Church JA, Clark PU, Cazenave A, Gregory J, et al (2013b) Sea Level Change Supplementary Material. In: *Climate Change 2013: The Physical Science Basis. Contribution of Working Group I to the Fifth Assessment Report of the Intergovernmental Panel on Climate Change* [Stocker, T.F., D. Qin, G.-K. Plattner,

- M. Tignor, S.K. Allen, J. Boschung, A. Nauels, Y. Xia, V. Bex and P.M. Midgley (eds.)]. Available from [www.climatechange2013.org](http://www.climatechange2013.org) and [www.ipcc.ch](http://www.ipcc.ch).
17. Ciuffardi T, Napolitano E, Iacono R, Reseghetti F, Raiteri G, Bordone A (2016) Analysis of surface circulation structures along a frequently repeated XBT transect crossing the Ligurian and Tyrrhenian seas. *Ocean Dyn.* 66 (6–7): 767–783.
  18. Collins WJ, Bellouin N, Doutriaux-Boucher M, Gedney N, Halloran P, Hinton T, Hughes J, Jones CD et al (2011) Development and evaluation of an Earth-System model – HadGEM2. *Geoscient Model Dev* 4:1051–1075. [https:// doi.org/10.5194/gmd-4-1051-2011](https://doi.org/10.5194/gmd-4-1051-2011)
  19. Dangendorf S, Hay C, Calafat FM, Marcos M, Piecuch CG, Berk K, and Jensen J (2019) Persistent acceleration in global sea-level rise since the 1960s. *Nature Climate Change* 9:705-710
  20. Dee D, Uppala S, Simmons A, Berrisford P, Poli P, Kobayashi S et al (2011) The ERA-Interim reanalysis: Configuration and performance of the data assimilation system. *Q. J. R. Meteorol. Soc.* 137:553–597. doi: 10.1002/qj.828
  21. Egbert GD, Erofeeva SY (2002) Efficient inverse modeling of barotropic ocean tides. *Journal of Atmospheric and Oceanic Technology* 19:183–204. doi:10.1175/1520-0426(2002)019;0183:EIMOBO;2.0.CO;2.
  22. Escudier R, Clementi E, Omar M et al (2020) Mediterranean Sea Physical Reanalysis (CMEMS MED-Currents) (Version 1). Copernicus Monitoring Environment Marine Service (CMEMS). [https://doi.org/10.25423/CMCC/MEDSEA\\_MULTIYEAR\\_PHY\\_006\\_004\\_E3R1](https://doi.org/10.25423/CMCC/MEDSEA_MULTIYEAR_PHY_006_004_E3R1)
  23. Frederikse T, Landerer F, Caron L, Adhikari S et al (2020) The causes of sea-level rise since 1900. *Nature* 584:393–397
  24. Fox-Kemper B, Menemenlis D (2008) Can large eddy simulation techniques improve mesoscale rich ocean models? *Geophys Monogr*:319–337
  25. García-Lafuente J, Alvarez-Fanjul E, Vargas J, Ratsimandresy A (2002) Subinertial variability through the Strait of Gibraltar. *J Geophys Res* 107(C10):3168. doi:10.1029/2001JC001104
  26. García-Lafuente J, Sammartino S, Huertas IE, Flecha S, Sánchez-Leal RF, Naranjo C, Nadal I and Bellanco MJ (2021) Hotter and Weaker Mediterranean Outflow as a Response to Basin-Wide Alterations. *Front. Mar. Sci.* 8:613444. doi: 10.3389/fmars.2021.613444
  27. Gaspar P, Gregoris Y, Lefevre JM (1990) A simple eddy kinetic energy model for simulations of the oceanic vertical mixing: Tests at station Papa and long-term upper ocean study site. *Journal of Geophysical Research* 95 16179. doi:10.1029/jc095ic09p16179.
  28. Gill AE, and Niller PP (1973) The theory of the seasonal variability in the ocean. *Deep-Sea Res. Oceanogr. Abstr.* 20: 141– 177, doi:10.1016/0011-7471(73)90049-1.
  29. Giorgi F, Jones C, Asrar GR (2009) Addressing climate information needs at the regional level: the CORDEX framework. *WMO Bull* 58(3)
  30. Gökaşan E, Tur H, Ecevitoglu B, Görüm T, Türker A, Tok B, Çağlak F, Birkan H, Şimşek M (2005) Evidence and implications of massive erosion along the Strait of İstanbul (Bosphorus). *Geo-Mar Lett* 25: 324–342
  31. Gökaşan E, Ergin M et al (2007) Factors controlling the morphological evolution of the Çanakkale Strait (Dardanelles, Turkey). *Geo-Mar Lett* 28:107–129

32. Greatbatch RJ (1994) A note on the representation of steric sea level in models that conserve volume rather than mass. *J. Geophys. Res.* 99(C6):12767–12771.
33. Gregory JM, Griffies SM, Hughes CW et al (2019) Concepts and terminology for sea level: mean, variability and change, both local and global. *Surv Geophys* 40:1251–1289 <https://doi.org/10.1007/s10712-019-09525-z>
34. Griffies SM, Greatbatch RJ (2012) Physical processes that impact the evolution of global mean sea level in ocean climate models. *Ocean Modell.* 51:37–72, doi:10.1016/j.ocemod.2012.04.003
35. Hamlington BD, Thompson P, Hammond WC, Blewitt G, and Ray RD (2016) Assessing the impact of vertical land motion on twentieth century global mean sea level estimates, *J. Geophys. Res. Oceans* 121:4980– 4993, doi:10.1002/2016JC011747.
36. Hermans THJ, Tinker J, Palmer MD et al (2020) Improving sea-level projections on the Northwestern European shelf using dynamical downscaling. *Clim Dyn* 54:1987–2011. <https://doi.org/10.1007/s00382-019-05104-5>
37. Holgate SJ, Matthews A, Woodworth PL, Rickards LJ, Tamisiea ME, Bradshaw E, Foden PR, Gordon KM, Jevrejeva S, and Pugh J (2013) New data systems and products at the Permanent Service for Mean Sea Level. *Journal of Coastal Research* 29(3):493–504 (DOI: 10.2112/JCOASTRES-D-12-00175.1).
38. Iacono R, Napolitano E (2020) Aspects of the summer circulation in the eastern Ligurian Sea, *Deep Sea Research Part I: Oceanographic Research Papers*, Volume 166, 103407, ISSN 0967-0637, <https://doi.org/10.1016/j.dsr.2020.103407>
39. IPCC (2013) Summary for Policymakers. In: *Climate Change 2013: The Physical Science Basis. Contribution of Working Group II to the Fifth Assessment Report of the Intergovernmental Panel on Climate Change.* Cambridge University Press: Cambridge and New York, USA and UK, 2014, available online: [https://www.ipcc.ch/site/assets/uploads/2018/02/WG1AR5\\_all\\_final.pdf](https://www.ipcc.ch/site/assets/uploads/2018/02/WG1AR5_all_final.pdf).
40. IPCC (2019) Technical Summary [H.-O. Pörtner, D.C. Roberts, V. Masson-Delmotte, P. Zhai, E. Poloczanska, K. Mintenbeck, M. Tignor, A. Alegría, M. Nicolai, A. Okem, J. Petzold, B. Rama, N.M. Weyer (eds.)]. In: *IPCC Special Report on the Ocean and Cryosphere in a Changing Climate* [H.- O. Pörtner, D.C. Roberts, V. Masson-Delmotte, P. Zhai, M. Tignor, E. Poloczanska, K. Mintenbeck, A. Alegría, M. Nicolai, A. Okem, J. Petzold, B. Rama, N.M. Weyer (eds.)], <https://www.ipcc.ch/srocc/>
41. Jeftic L, Milliman JD and Sestini, G (1992) Climatic change and the Mediterranean: environmental and societal impacts of climatic change and sea-level rise in the Mediterranean region. United Nations Environment Programme, <http://hdl.handle.net/20.500.11822/29285>
42. Jordà G, Gomis D (2013) On the interpretation of the steric and mass components of sea level variability: The case of the Mediterranean basin. *J. Geophys. Res. Oceans* 118:953– 963, doi:10.1002/jgrc.20060.
43. Jordà G, Von Schuckmann K, Josey SA, Caniaux G et al (2017a) The Mediterranean Sea heat and mass budgets: Estimates, uncertainties and perspectives. *Progress in Oceanography* 156:174–208. doi:10.1016/j.pocean.2017.07.001
44. Jordà G, Sánchez-Román A, Gomis D (2017b) Reconstruction of transports through the Strait of Gibraltar from limited observations. *Clim Dyn* 48:851–865, <https://doi.org/10.1007/s00382-016-3113-8>
45. Kara AB, Wallcraft AJ, Hulbert HE, Stanev EV (2008) Air-sea fluxes and river discharges in the Black Sea with a focus on the Danube and Bosphorus. *J. Mar. Syst.* 74:74–95.

46. King MD, Howat IM, Candela SG, Noh MJ et al (2020) Dynamic ice loss from the Greenland Ice Sheet driven by sustained glacier retreat. *Commun Earth Environ* 1, 1. <https://doi.org/10.1038/s43247-020-0001-2>
47. Klein B, Roether W, Manca BB, Bregant D, Beitzel V, Kovacevic V, Luchetta A (1999) The large deep water transient in the Eastern Mediterranean. *Deep Sea Research Part I* 46: 371-414.
48. Knysh, VV, Demyshev SG, Korotaev GK (2002) Method of reconstructing the climatic seasonal circulation of the Black Sea on the basis of assimilation of hydrologic data in models. *Marine Hydrophys. J.* 2:36–52, (in Russian).
49. Kubryakov AA, Stanichny SV (2011) Mean Dynamic Topography of the Black Sea, computed from altimetry, drifter measurements and hydrology data. *Ocean Sci.* 7:745–753. <https://doi.org/10.5194/os-7-745-2011>
50. Lambeck K, Smither C, Johnston P (1998) Sea-level change, glacial rebound and mantle viscosity for northern Europe. *Geophys. J. Int.* 134:102–144.
51. Lambeck K, Yokoyama Y, Purcell A, Johnston P (2002) Reply to the comment by WR Peltier. *Quaternary Science Reviews*, 21:415-418.
52. Landerer FW, Volkov DL (2013) The anatomy of recent large sea level fluctuations in the Mediterranean Sea. *Geophys. Res. Lett.* 40:553–557
53. Large WG, Yeager SG (2004) Diurnal to decadal global forcing for ocean and sea-ice models: the data sets and flux climatologies. National Center for Atmospheric Research Boulder. <http://dx.doi.org/10.5065/D6KK98Q6>
54. Leith C (1968) Parameterization of vertical mixing in numerical models of tropical oceans. *Phys Fluids* 10:1409–1416
55. Llasses J, Jordà G, Gomis D, Adloff F et al (2018) Heat and salt redistribution within the Mediterranean Sea in the Med-CORDEX model ensemble. *Clim. Dyn.* 51:1119-1143.
56. Losch M, Adcroft A, Campin JM (2004) How sensitive are coarse general circulation models to fundamental approximations in the equations of motion? *J. Phys. Oceanogr.*, 34:306–319.
57. Marullo S, Buongiorno Nardelli B, Guarracino M, Santoleri R (2007) Observing the Mediterranean Sea from space: 21 years of Pathfinder-AVHRR sea surface temperatures (1985 to 2005): re-analysis and validation. *Ocean Sci.* 3: 299-310
58. Meinshausen M, Smith SJ, Calvin K, Daniel JS, Kainuma MLT, Lamarque JF, Matsumoto K, Montzka SA, Raper SCB, Riahi K, Thomson A, Velders GJM, van Vuuren DPP (2011) The RCP greenhouse gas concentrations and their extensions from 1765 to 2300. *Clim Change* 109:210–241. <https://doi.org/10.1007/s10584-011-0156-z>
59. Marcos M, Tsimplis MN (2008) Coastal sea level trends in Southern Europe. *Geophys. J. Int.* 175:70–82.
60. Marshall J, Hill C, Perelman L, Adcroft A (1997a) Hydrostatic, quasi-hydrostatic, and nonhydrostatic ocean modeling. *J Geophys Res* 102:5733–5752
61. Marshall J, Adcroft A, Hill C, Perelman L, Heisey C (1997b) A finite-volume, incompressible Navier Stokes model for studies of the ocean on parallel computers. *J Geophys Res* 102:5753–5766

62. Meyssignac B, Calafat FM, Somot S, Rupolo V, Stocchi P, Llovel W, Cazenave A (2011) Two-dimensional reconstruction of the mediterranean sea level over 1970–2006 from tide gage data and regional ocean circulation model outputs. *Glob. Planet. Change* 77(1–2): 49–61.
63. Mohamed B, Mohamed A et al (2019) Inter-Annual Variability and Trends of Sea Level and Sea Surface Temperature in the Mediterranean Sea over the Last 25 Years. *Pure Appl. Geophys.* 176:3787–3810.
64. Naranjo C, Garcia-Lafuente J, Sannino G, Sanchez-Garrido JC (2014) How much do tides affect the circulation of the Mediterranean Sea? From local processes in the Strait of Gibraltar to basin-scale effects, *Progress in Oceanography* 127:108-116 /doi.org/10.1016/j.pocean.2014.06.005.
65. Palma M, Iacono R, Sannino G, Bargagli A, Carillo A, Fekete BM, Lombardi E, Napolitano E, Pisacane G, Struglia MV (2020) Short-term, linear and non-linear local effects of the tides on the surface dynamics in a new, high-resolution model of the Mediterranean Sea circulation. *Ocean Dyn.* 70:935-963 <https://doi.org/10.1007/s10236-020-01364-6>.
66. Peltier WR (2002) Comments on the paper of Yokoyama et al. (2000) entitled "Timing of the Last Glacial Maximum from observed sea level minima". *Quaternary Science Reviews* 21:409-414
67. Peltier WR (2004) Global glacial isostasy and the surface of the ice-age earth: The ICE-5G (VM2) model and GRACE. *Annu. Rev. Earth Planet. Sci.* 32:111–149 doi:10.1146/annurev.earth.32.082503.144359.
68. Peneva E, Stanev E, Belokopytov V, Le Traon PY (2001) Water transport in the Bosphorus Strait estimated from hydro-meteorological and altimeter data: Seasonal and decadal variability. *J. Mar. Syst.* 31:21–33.
69. Pinardi N, Zavatarelli M, Adani M, Coppini G, Fratianni C, Oddo P, Simoncelli S, Tonani M, Lyubartsev V, Dobricic S, Bonaduce A (2015) Mediterranean Sea large-scale low-frequency ocean variability and water mass formation rates from 1987 to 2007: a retrospective analysis. *Prog Oceanogr.*, 132: 318-332. <https://doi.org/10.1016/j.pocean.2013.11.003>.
70. Ponce VM (1994) *Engineering hydrology: principles and practices*. Prentice Hall
71. Poulain PM, Mauri E, Gerin R, Chiggiato J et al (2020) On the dynamics in the southeastern Ligurian Sea in summer 2010. *Cont. Shelf Res.* 196:104083
72. Rahmstorf S (2007) A semi-empirical approach to projecting future sea-level rise, *Science* 315(8010): 368-370, doi: 10.1126/science.1135456.
73. Rio MH, Pascual A, Poulain PM, Menna M, Barcelo' B, Tintoré J (2014) Computation of a new mean dynamic topography for the Mediterranean Sea from model outputs, altimeter measurements and oceanographic in situ data. *Ocean Sci.* 10:731-744.
74. Roether W, Manca BB, Klein B et al (1996) Recent changes in eastern Mediterranean deep waters. *Science* 271: 333–335. doi:10.1126/science.271.5247.333.
75. Sánchez Román A, Sannino G, García Lafuente J et al (2009) Transport estimates at the western section of the Strait of Gibraltar: A combined experimental and numerical modeling study. *Journal of Geophysical Research: Oceans* 114, C06002. <https://doi.org/10.1029/2008JC005023>.
76. Sannino G, Sözer A, Özsoy E (2017) A high-resolution modelling study of the Turkish Straits System. *Ocean Dynamics* 67(3):397–432
77. Sannino G, Carillo A, Pisacane G, Naranjo C (2015) On the relevance of tidal forcing in modelling the Mediterranean thermohaline circulation. *Prog Oceanogr* 134:304–329

78. Sannino G, Herrmann M, Carillo A, Rupolo V, Ruggiero V, Artale V, Heimbach P (2009) An eddy-permitting model of the Mediterranean sea with a two-way grid refinement at the Strait of Gibraltar. *Ocean Modelling* 30 (1): 56–72
79. Sannino G, Carillo A, Pratt L (2009) Hydraulic criticality of the exchange flow through the strait of Gibraltar. *Journal of Physical Oceanography* 39:2779–2799. doi:10.1175/2009JPO4075.1
80. Santamaría-Gómez, A, Gravelle M, Dangendorf S, Marcos M, Spada G, Wöppelmann G (2017) Uncertainty of the 20th century sea-level rise due to vertical land motion errors. *Earth and Planetary Science Letters* 473:24-32. <https://doi.org/10.1016/j.epsl.2017.05.038>.
81. Sanz JL, Acosta J, Esteras M, Herranz P, Palomo C, Sandoval N (1991) Prospección geofísica del Estrecho de Gibraltar: resultados del Programa Hércules (1980–1983). Publ. espec. Inst. Esp. Oceanogr. Span. Inst. of Oceanogr., Madrid
82. Sen Gupta A, Jourdain NC, Brown JN, Monselesan D (2013) Climate drift in the CMIP5 models. *J. Climate* 26:8597– 8615. doi:10.1175/JCLI-D-12-00521.1.
83. Shugar DH, Burr A, Haritashya UK et al (2020) Rapid worldwide growth of glacial lakes since 1990. *Nature Climate Change* 10:939-945. <https://doi.org/10.1038/s41558-020-0855-4>
84. Simonov AI, Altman EN (1991) Hydrometeorology and hydrochemistry of the USSR seas, in *Sensitivity to Change: Black Sea, Baltic Sea and North Sea*. NATO/ASI Ser., vol. IV, edited by E. Özsoy and A. Mikaelyan, pp. 11–25, Kluwer Acad., Dordrecht, Netherlands.
85. Slangen ABA, Adloff F, Jevrejeva S et al (2017a) Review of Recent Updates of Sea-Level Projections at Global and Regional Scales. *Surv. Geophys.*, 38:385–406.
86. Slangen ABA, Carson M, Katsman CA et al (2014) Projecting twenty-first century regional sea-level changes. *Climatic Change* 124:317–332. <https://doi.org/10.1007/s10584-014-1080-9>
87. Smagorinsky J (1963) General circulation experiments with the primitive equations. *Mon Weather Rev* 91:99–164
88. Soto-Navarro J, Criado-Aldeanueva F, Lafuente JG, Sanchez-Roman A (2010) Estimation of the Atlantic inflow through the Strait of Gibraltar from climatological and in situ data. *J. Geophys. Res.* 115. <https://doi.org/10.1029/2010JC006302>
89. Soto-Navarro J, Jordá, G, Amores A et al (2020) Evolution of Mediterranean Sea water properties under climate change scenarios in the Med-CORDEX ensemble. *Clim Dyn* 54:2135–2165. <https://doi.org/10.1007/s00382-019-05105-4>
90. Spada G, Stocchi P (2006) *The Sea Level Equation, Theory and Numerical Examples*, Aracne, Roma, p. 96, ISBN: 88–548–0384–7.
91. Spada G, Stocchi P (2007) SELEN: a Fortran 90 program for solving the ‘Sea Level Equation’. *Comput. Geosci.* 33(4): 538–562. doi:10.1016/j.cageo.2006.08.006.
92. Spada G (2017) Glacial Isostatic Adjustment and Contemporary Sea Level Rise: An Overview. *Surv Geophys* 38:153–185. <https://doi.org/10.1007/s10712-016-9379-x>
93. Strandberg G, Barring L, Hansson U, Jansson C, Jones C (2014) CORDEX scenarios for Europe from the Rossby Centre regional climate model RCA4.

94. Theocharis A, Klein B, Nittis K, Roether W (2002) Evolution and status of the Eastern Mediterranean Transient (1997–1999). *J. Mar. Syst.* 33-34: 91-116.
95. Thiéblemont R, Le Cozannet G, Toimil A, Meyssignac B, Losada IJ (2019) Likely and High-End Impacts of Regional Sea-Level Rise on the Shoreline Change of European Sandy Coasts Under a High Greenhouse Gas Emissions Scenario. *Water* 2019, 11, 2607.
96. Tsimplis MN, Josey SA (2001) Forcing of the Mediterranean Sea by atmospheric oscillations over the North Atlantic. *Geophysical Research Letters* 28:803-806. <https://doi.org/10.1029/2000GL012098>
97. Tsimplis MN, Bryden HL (2000) Estimation of the transports through the strait of Gibraltar. *Deep-Sea Res I* 47:2219–2242
98. Ünlüata Ü, Oğuz T, Latif MA, Özsoy E (1990) On the physical oceanography of the Turkish Straits, in *The Physical Oceanography of Sea Straits*. NATO/ASI Ser., edited by L. J. Pratt, pp. 25–60, Kluwer Acad., Dordrecht, Netherlands.
99. Vörösmarty CJ, Federer CA, Schloss AL (1998) Potential evaporation functions compared on US watersheds: implications for global-scale water balance and terrestrial ecosystem modeling. *J Hydrol* 207: 147–169
100. Vousdoukas MI, Mentaschi L, Voukouvalas E, Verlaan M, Feyen L (2017) Extreme sea levels on the rise along Europe's coasts. *Earth's Future* 5:304-323. <https://doi.org/10.1002/2016EF000505>
101. Wisser D, Frohking S, Douglas EM, Fekete BM, Vörösmarty CJ, Schumann AH (2008) Global irrigation water demand: variability and uncertainties arising from agricultural and climate data sets. *Geophys Res Lett* 35:L24408
102. Wisser D, Fekete BM, Vörösmarty CJ, Schumann AH (2010) Reconstructing 20th century global hydrography: a contribution to the Global Terrestrial Network- Hydrology (GTN-H). *Hydrol Earth Syst Sci* 14:1–24

## Figures

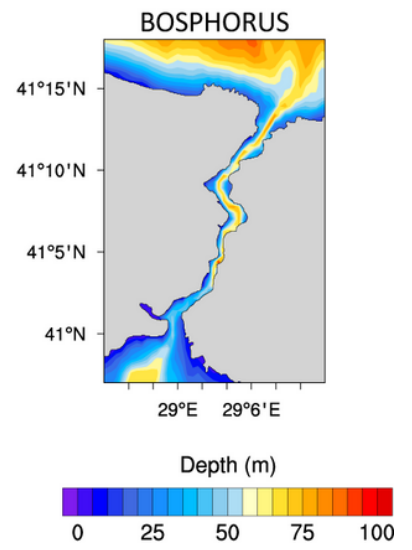
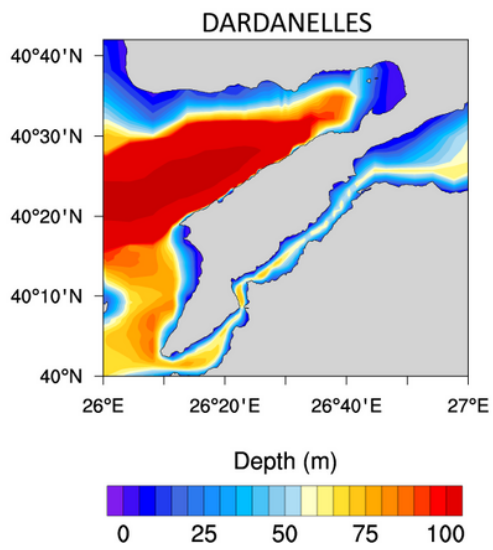
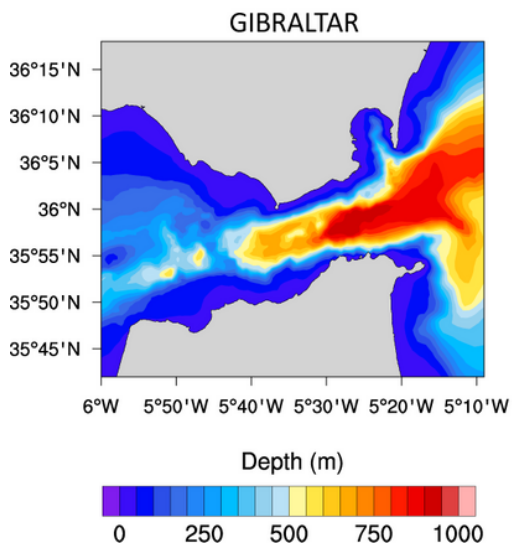
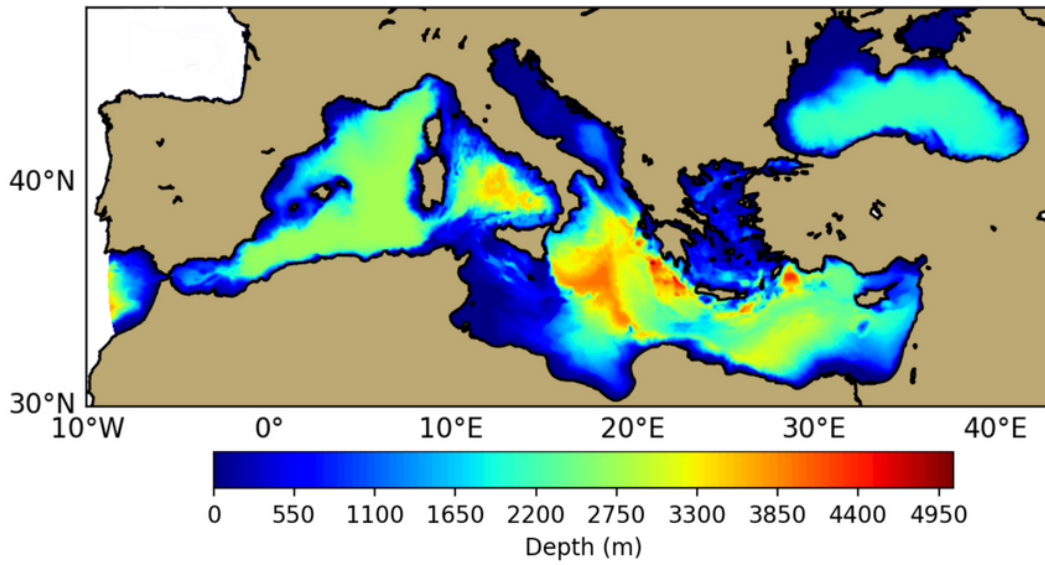


**Figure 1**

Model bathymetry: entire domain and high-resolution representation of the three straits (Gibraltar, Dardanelles, and Bosphorus) in which the spatial detail of the computational grid has been increased

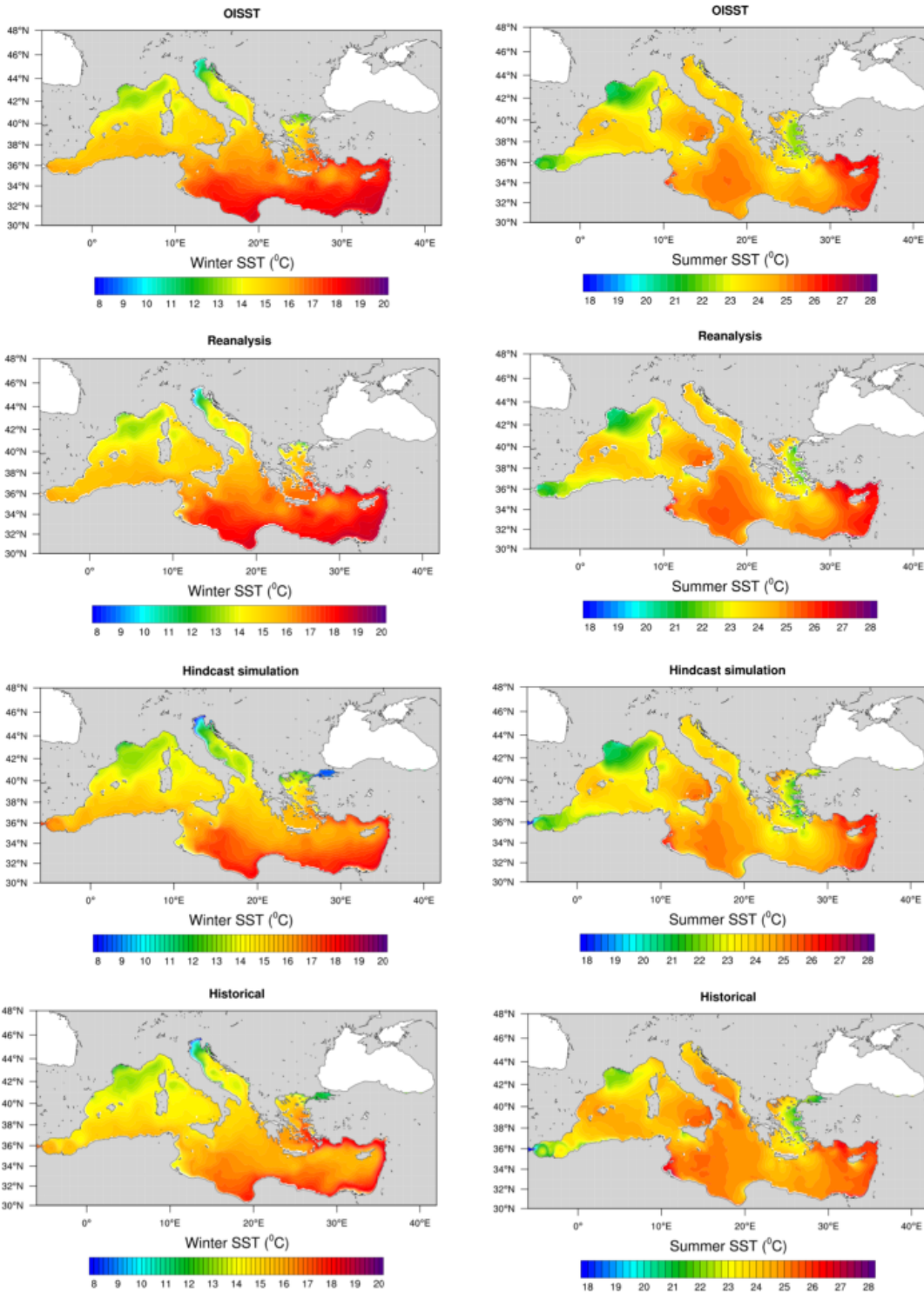


**Figure 2**

Map of the SST climatology for the OISST (a,b), COPERNICUS reanalysis (c,d), hindcast simulation (e,f), and historical simulation (g,h) over the common period 1987-2005. Winter (summer) climatologies are on the left (right) panels

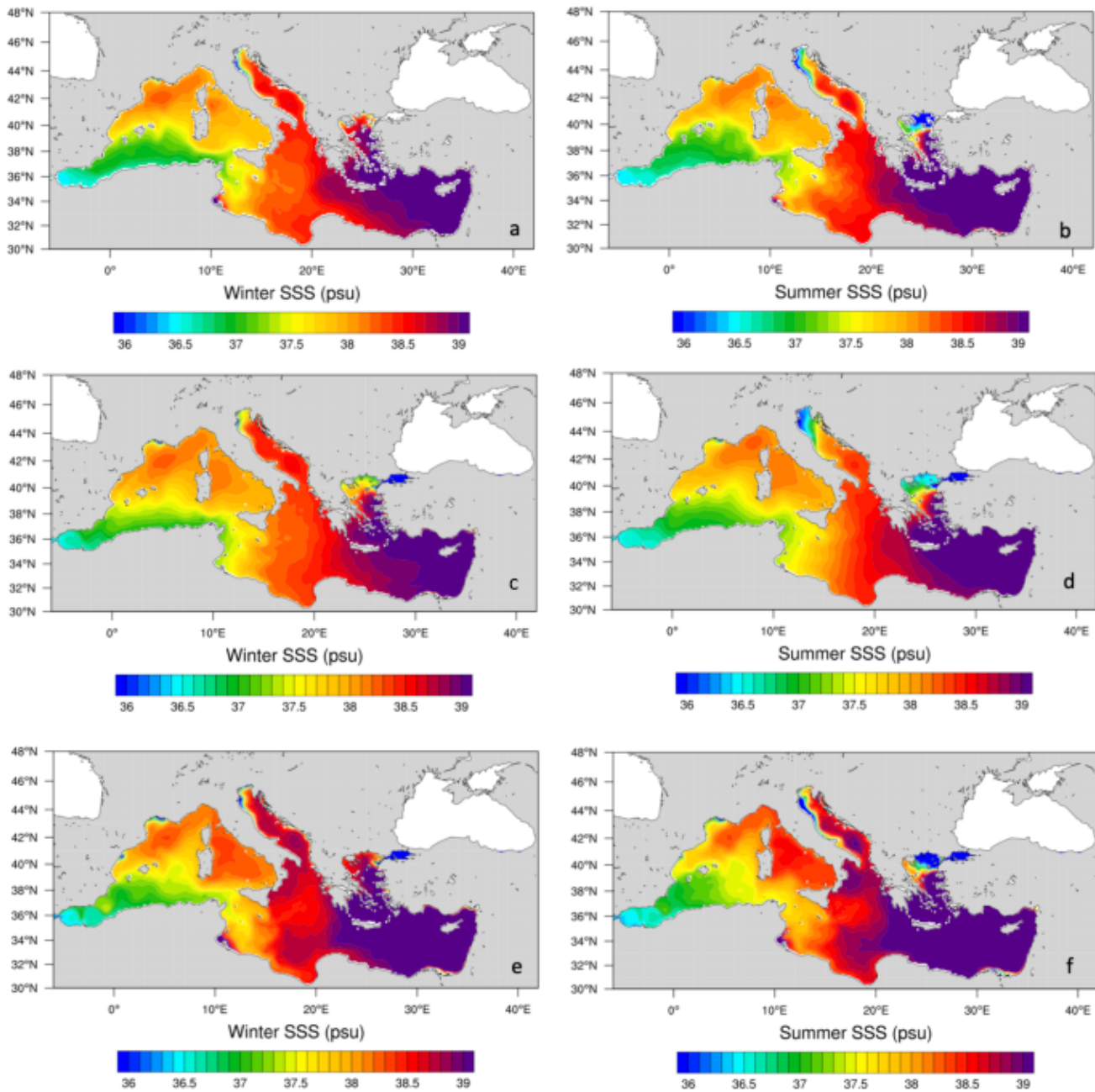


**Figure 3**

Map of the SSS climatology for COPERNICUS reanalysis (a,b), hindcast simulation (c,d), and historical simulation (e,f) over the common period 1987-2005. Winter (summer) climatologies are on the left (right) panels

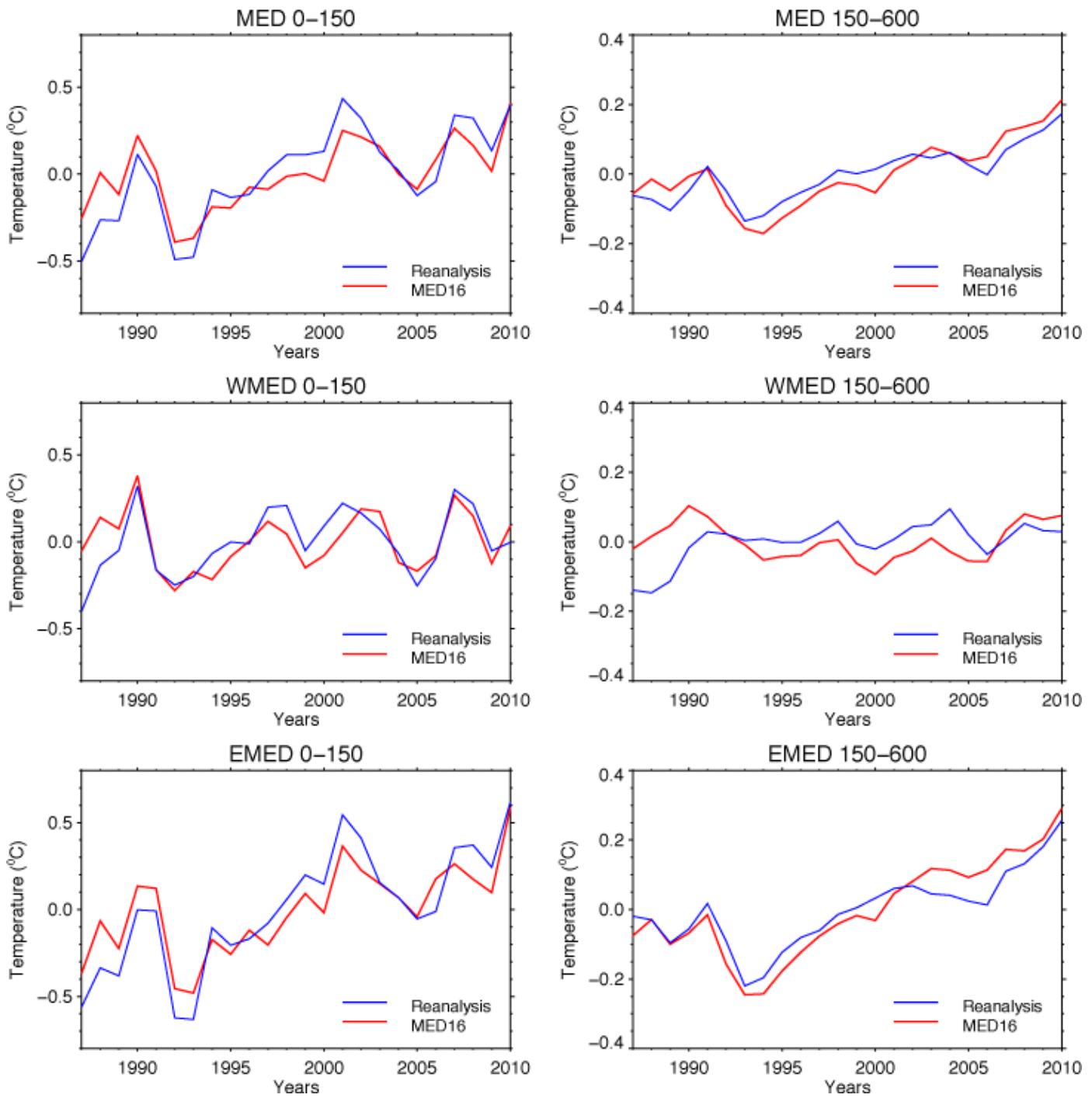


**Figure 4**

Reanalysis (blue) and hindcast (red) time series of temperature anomalies (°C ; annual values) for the upper (0-150 m) and intermediate (150-600 m) layers, for the Mediterranean Sea, and the western and eastern sub-basins

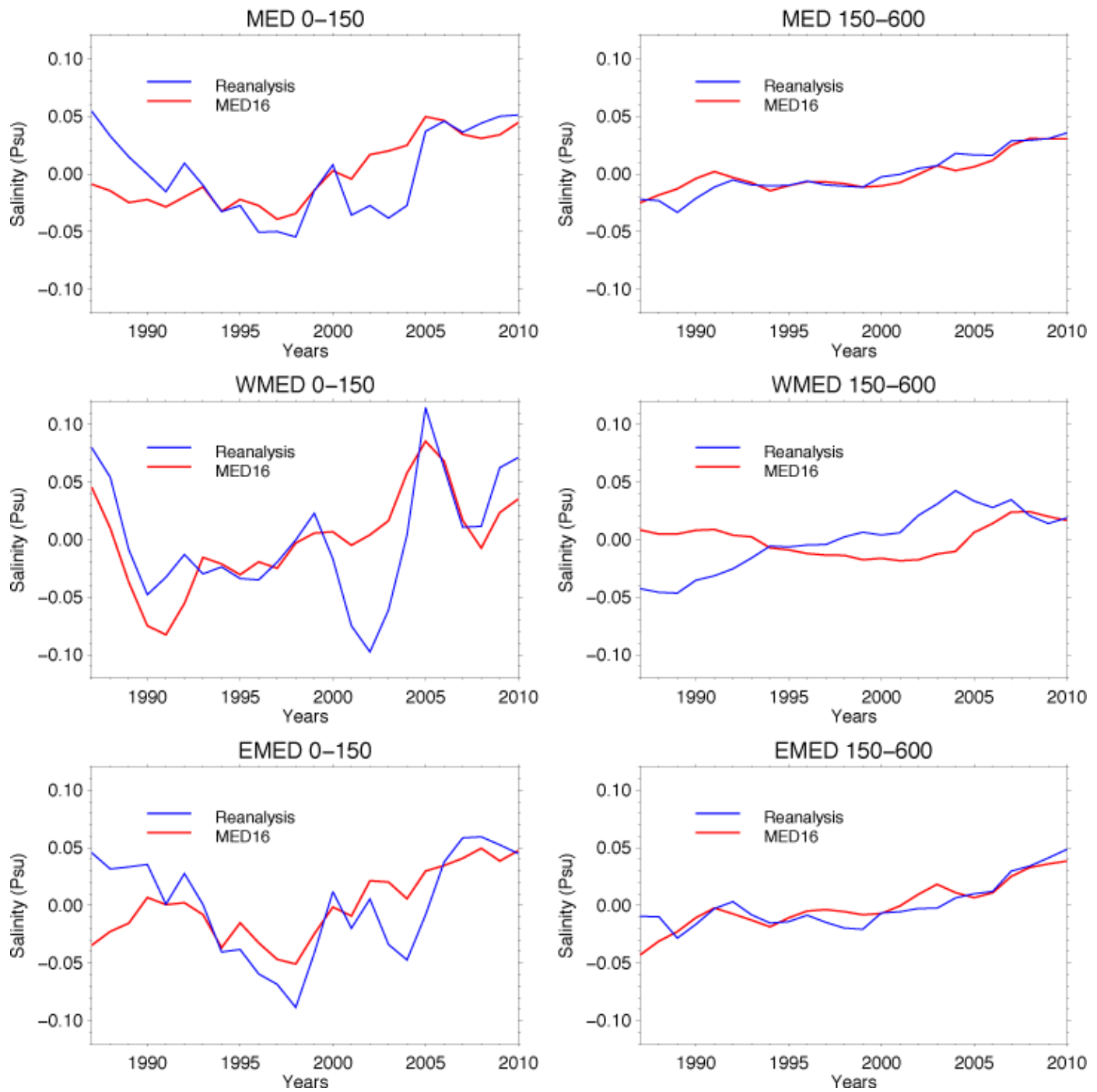


**Figure 5**

Reanalysis (blue) and hindcast simulation (red) time series of salinity anomalies (psu); annual values) for the upper (0-150 m) and intermediate (150-600 m) layers, for the Mediterranean Sea, and the western and eastern sub-basins

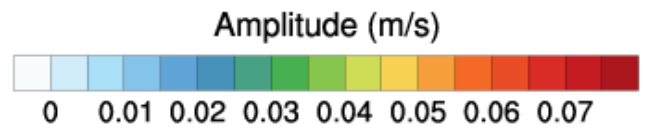
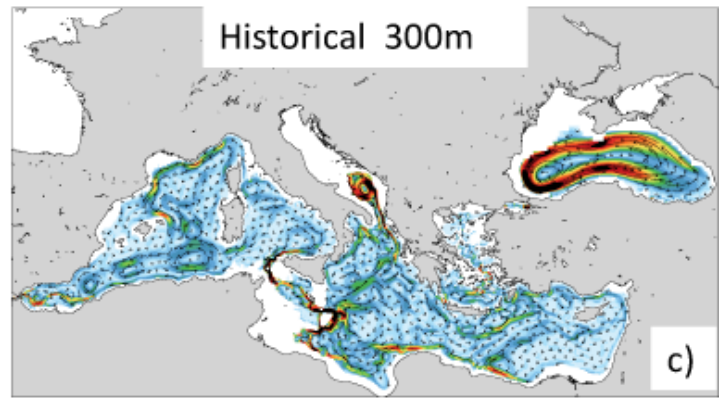
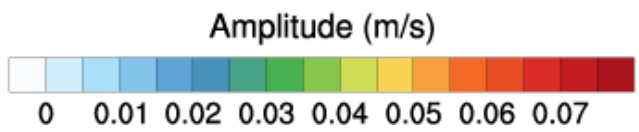
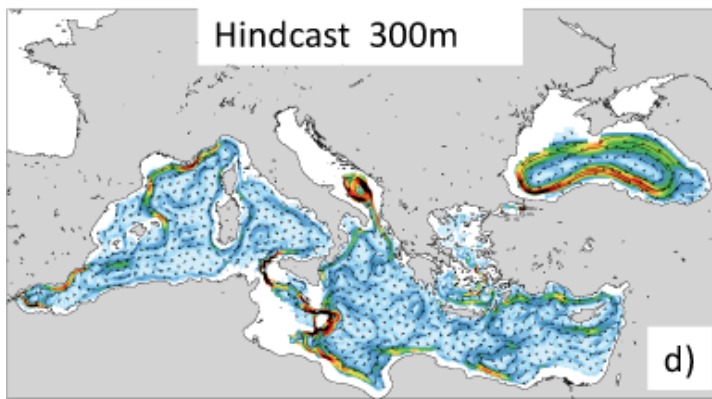
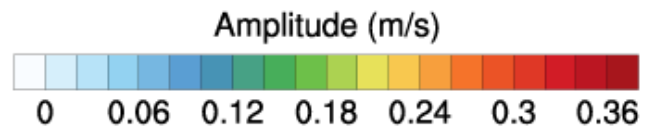
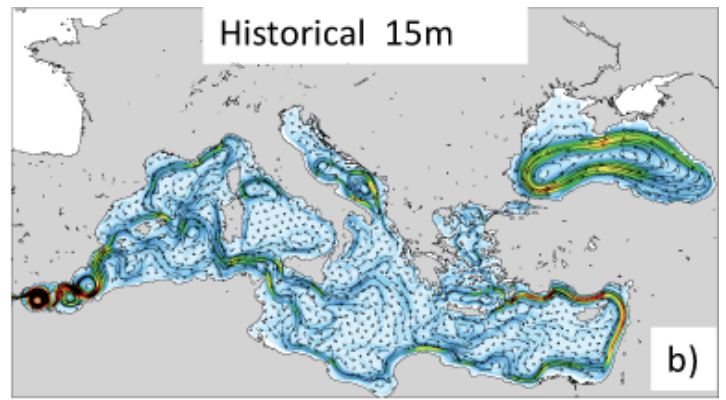
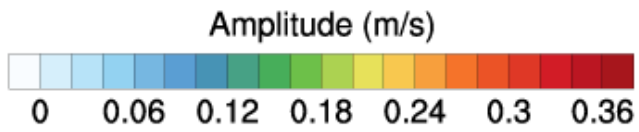
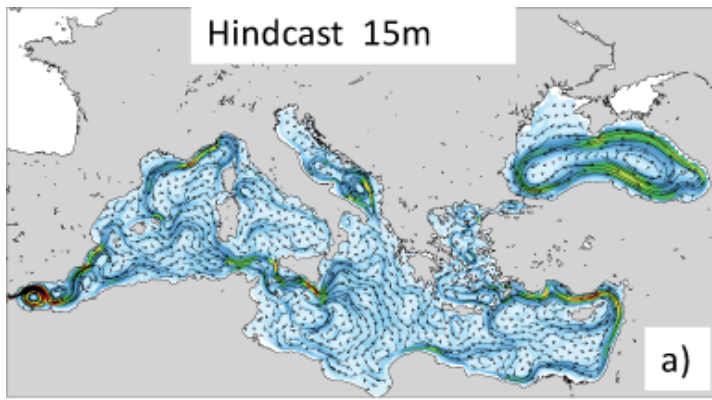


**Figure 6**

Surface (15 m of depth) and intermediate (300 m of depth) circulation, averaged over the simulation periods of the hindcast (left panel) and of the historical (right panel) experiments

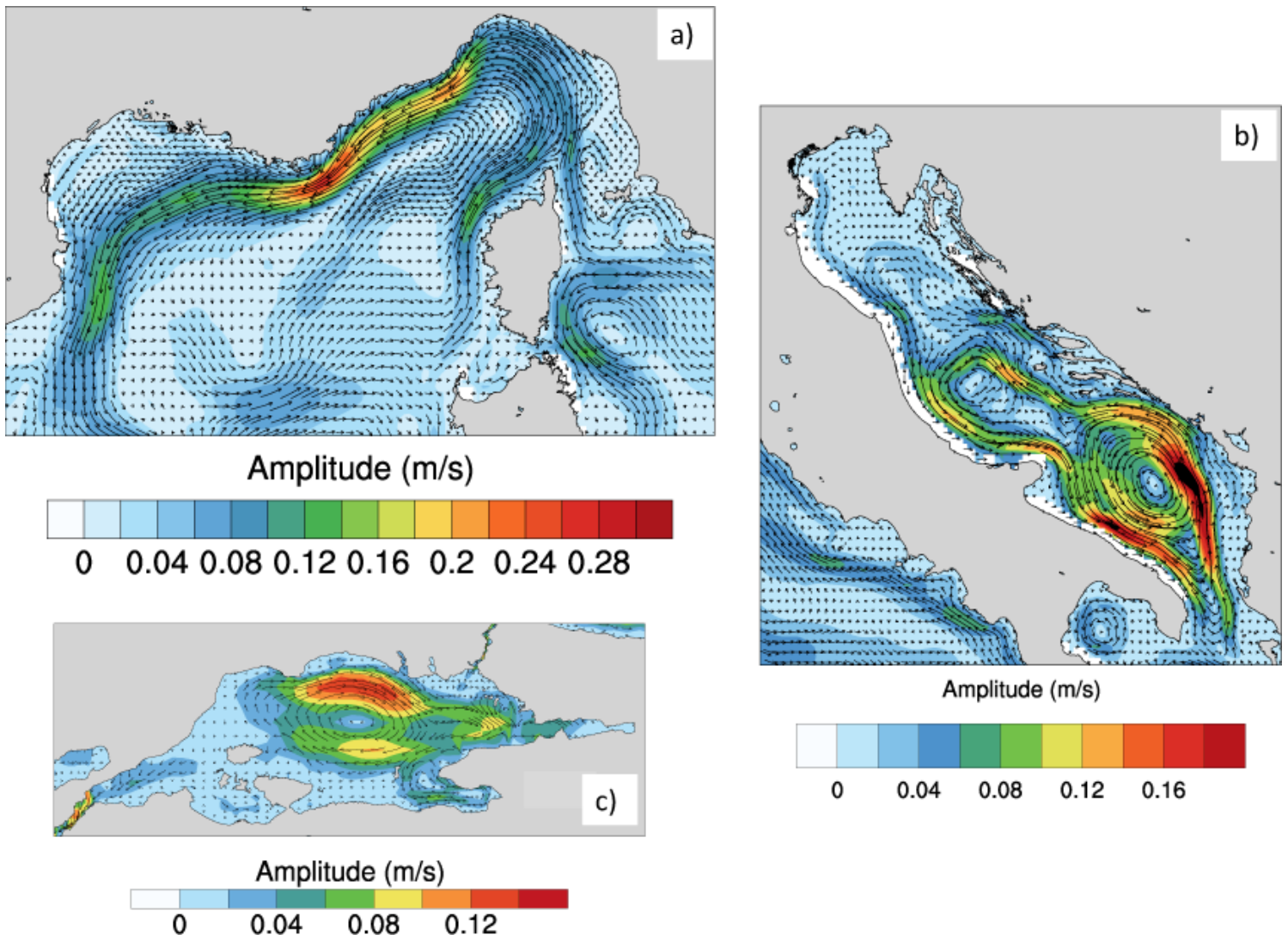


Figure 7

Hindcast surface (15 m of depth) circulation averaged over the simulation time-span (1982-2010) for three sub-basins: Liguro-Provençal (a), Adriatic (b), and Marmara Sea ©

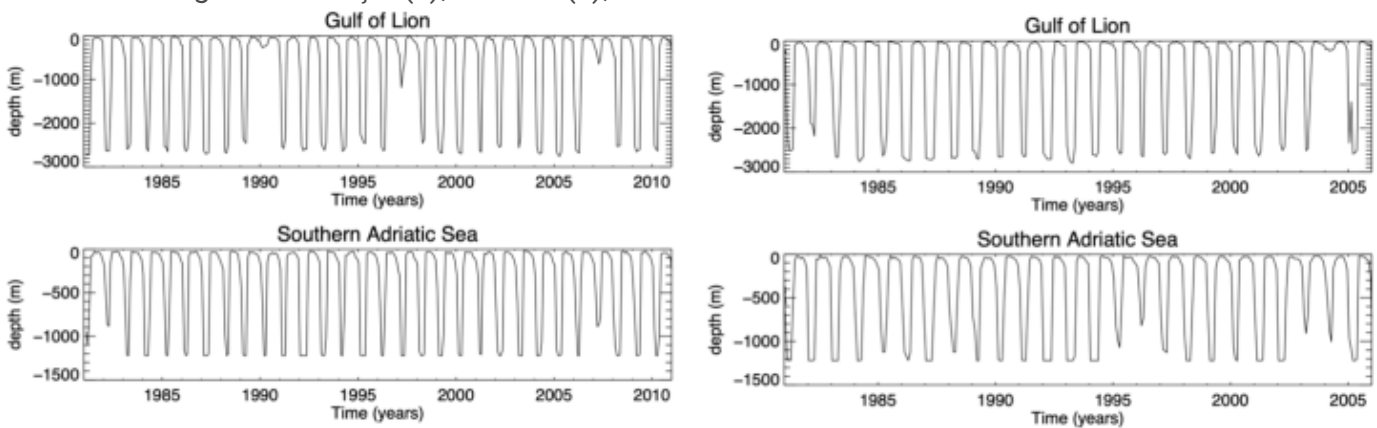
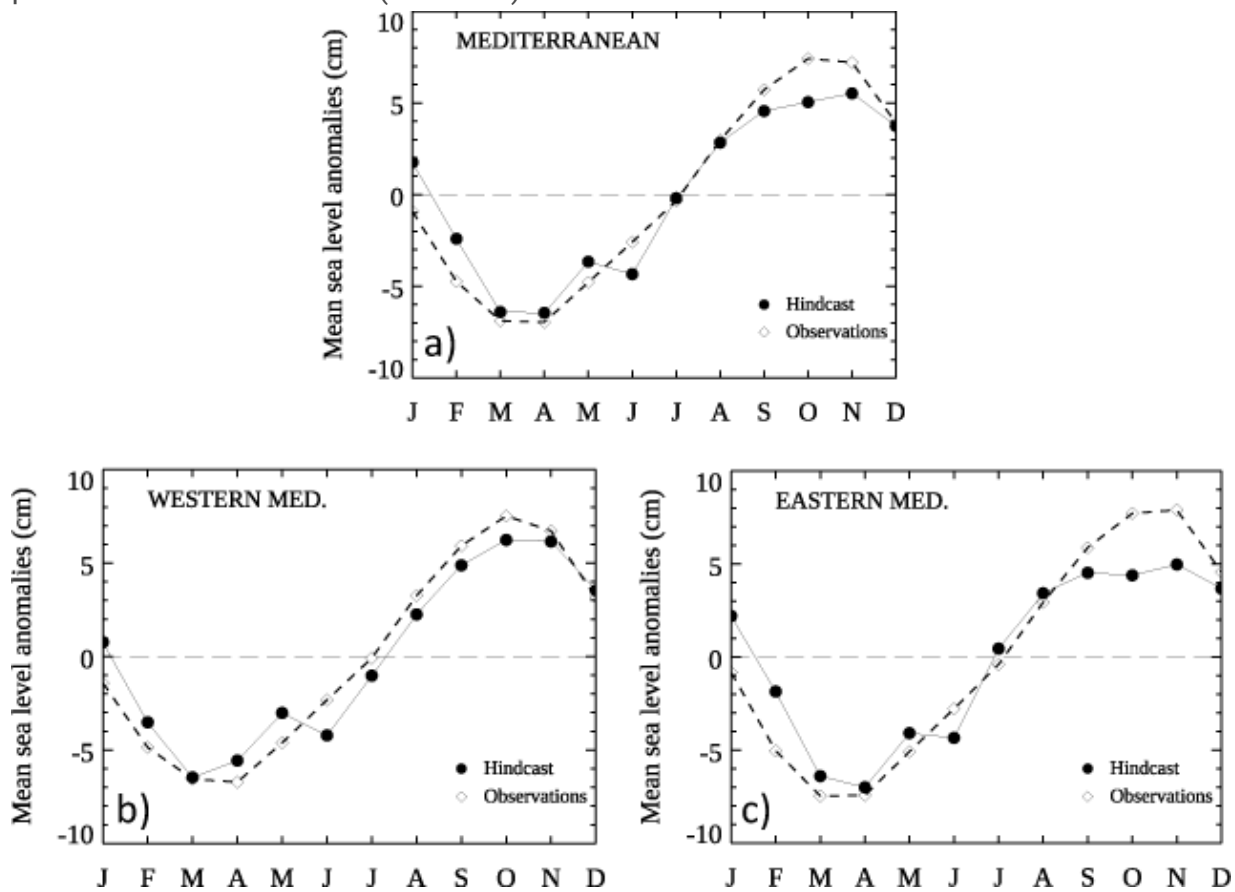


Figure 8

Time evolution of the monthly maximum MLD computed over the Gulf of Lion area (box from 3.34°E/39.97°N to 7.28°E/43.15°N) and the Southern Adriatic Sea (box from 16.47°E/40.28°N to 19.28°E/42.72°N). Left (right)

panels are for the hindcast (historical) simulation



**Figure 9**

Sea-level seasonal cycle; whole Mediterranean (panel a), western and eastern sub-basins (panels b-c). Black dots denote values computed from the hindcast simulation, and diamonds those from the observations

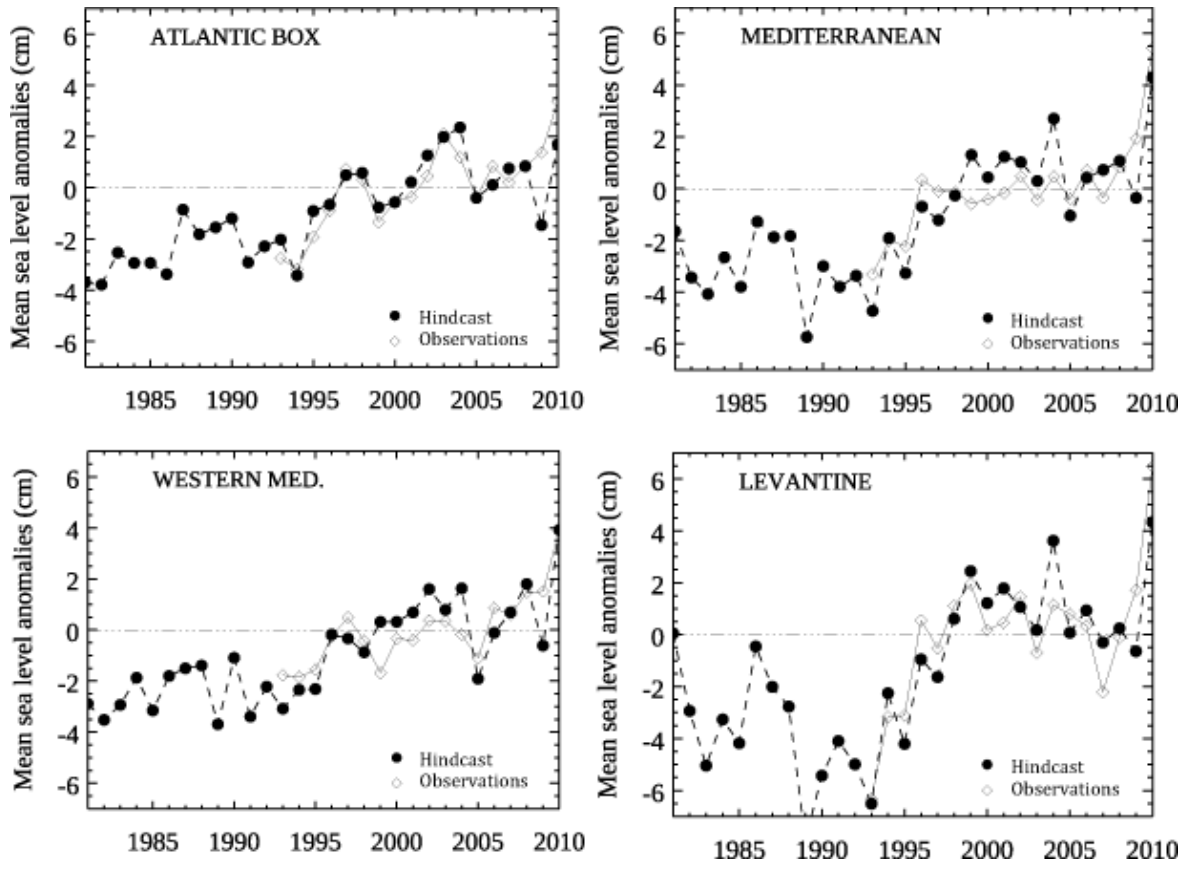
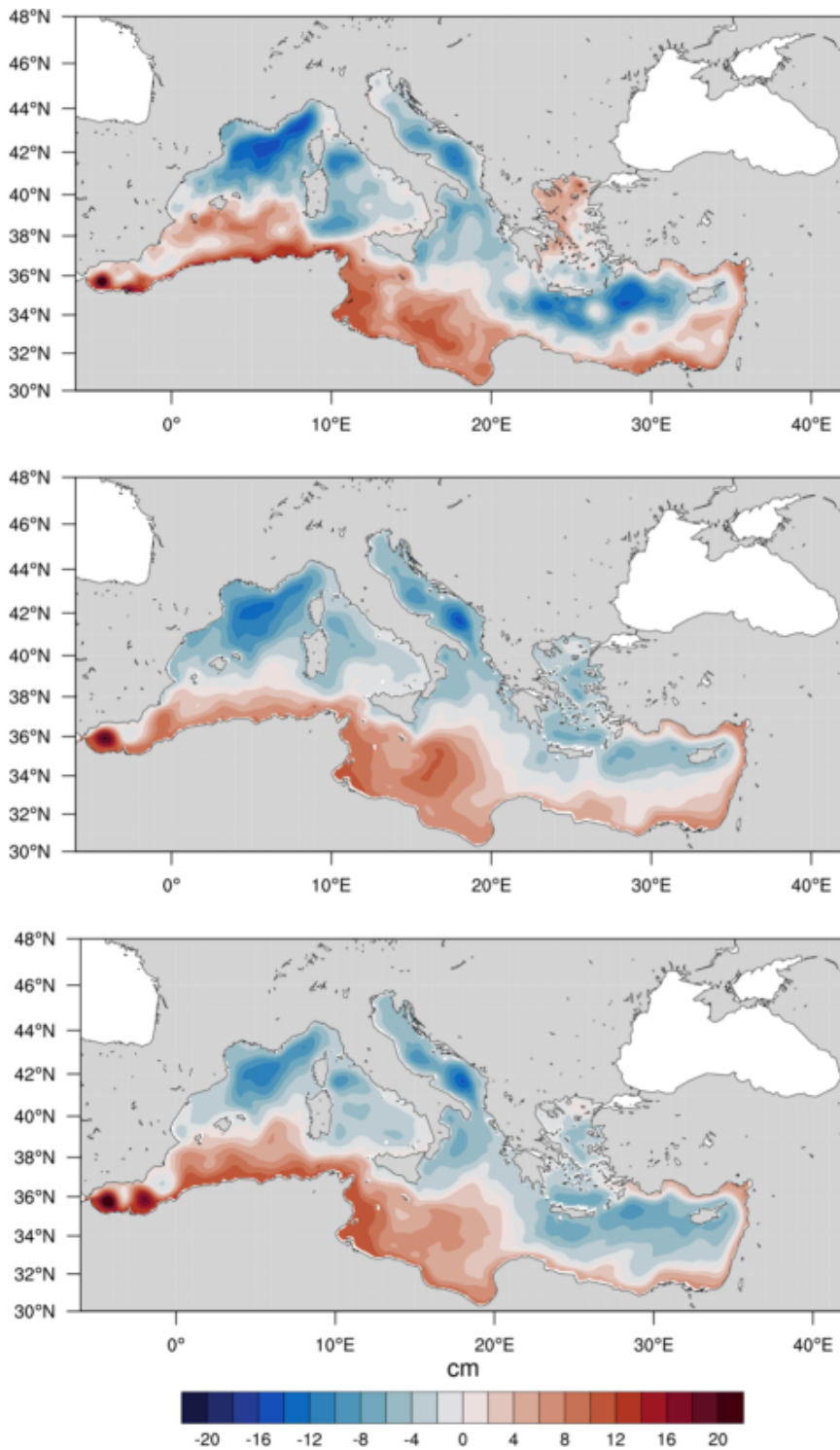


Figure 10

Interannual variability of the sea-level anomaly in different basins. Symbols are as in Figure 9



**Figure 11**

Averages of the SSH (1993-2010), for the hindcast (middle panel) and historical (lower panel) simulations, are compared with the average of the ADT for the same period (upper panel), which is very close to the mean dynamic topography. The historical simulation has been extended with the RCP8.5 scenario for 2006–2010. In all cases, the respective regional climatological means have been subtracted to ease the comparison of patterns

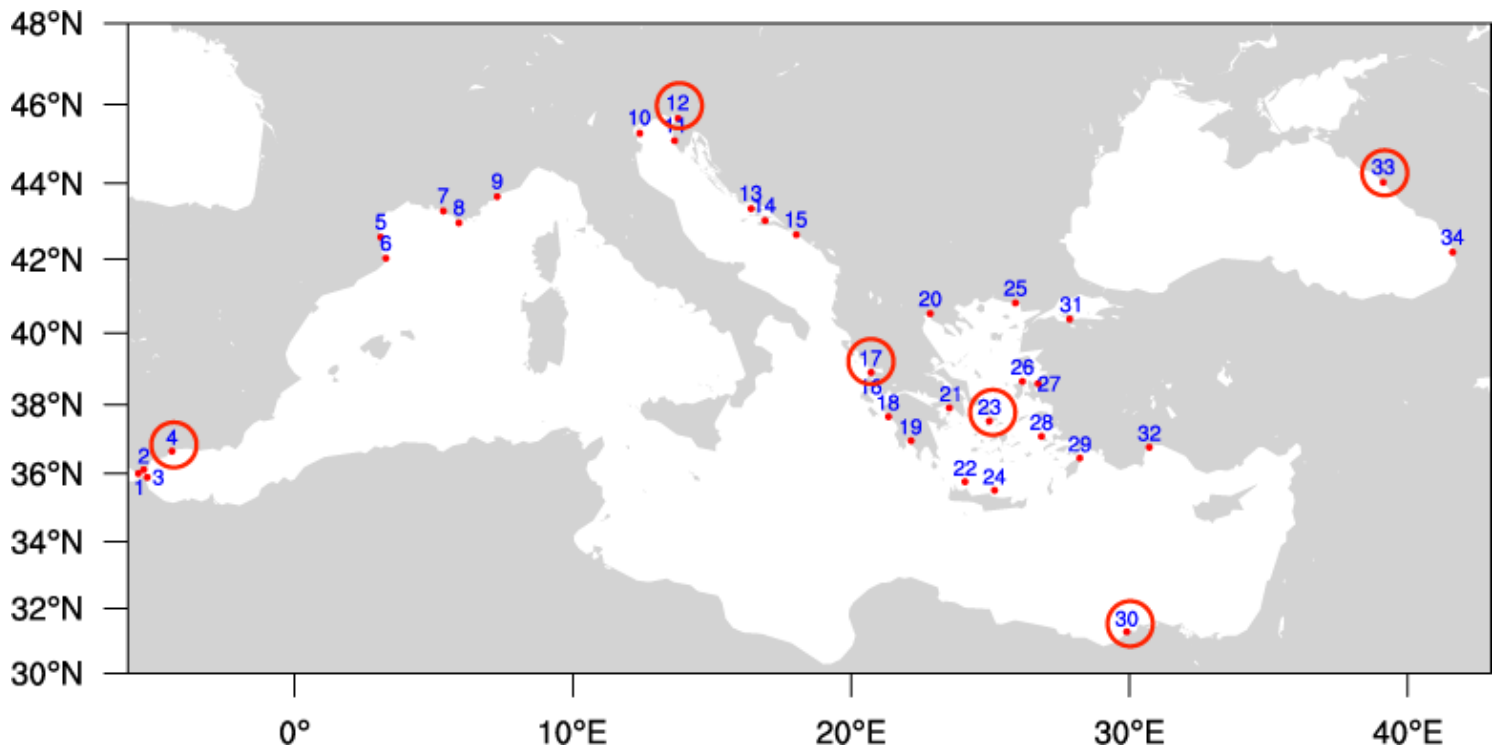


**Figure 12**

Location of the tide gauge stations whose data are used to construct Table 4. Red circles indicate stations used to extract the time series displayed in Figure 13

**Figure 13**

Comparison between sea-surface height time series extracted from the model (red) with tide gauge time series, at 6 locations along the coasts of the computational domain, marked by red circles in the map of Figure 12

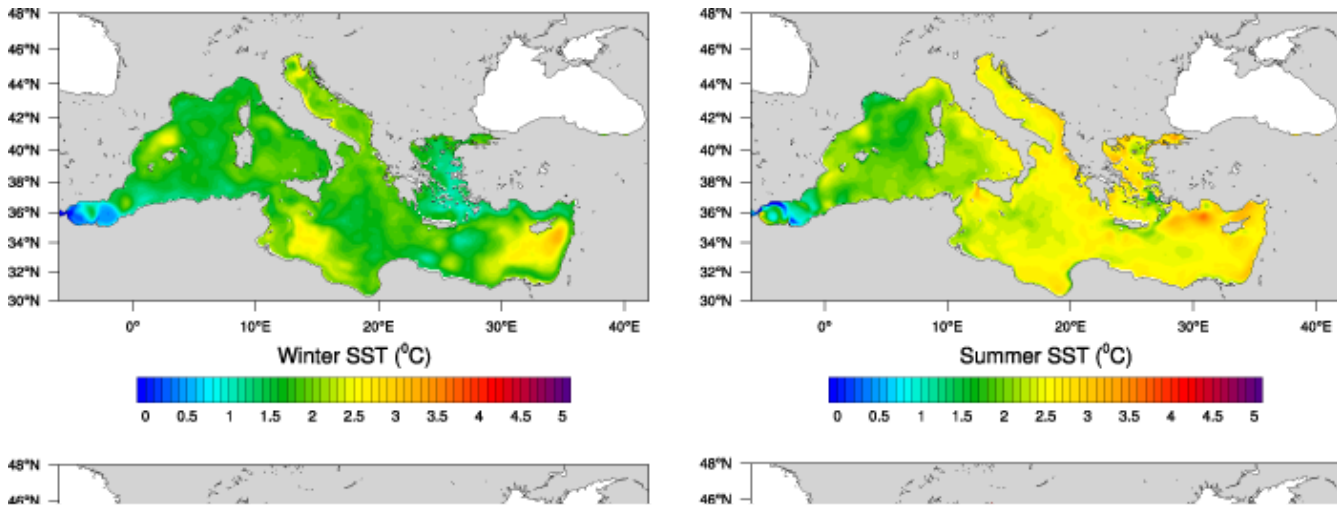


**Figure 14**

SST difference between averages over the scenario and the historical simulations for winter (left panels) and summer (right panels). Upper panels show averages over the period 2046-2065, lower panels over the period 2081-2100 (right panel). Historical simulation has been averaged over the entire period 1981-2005

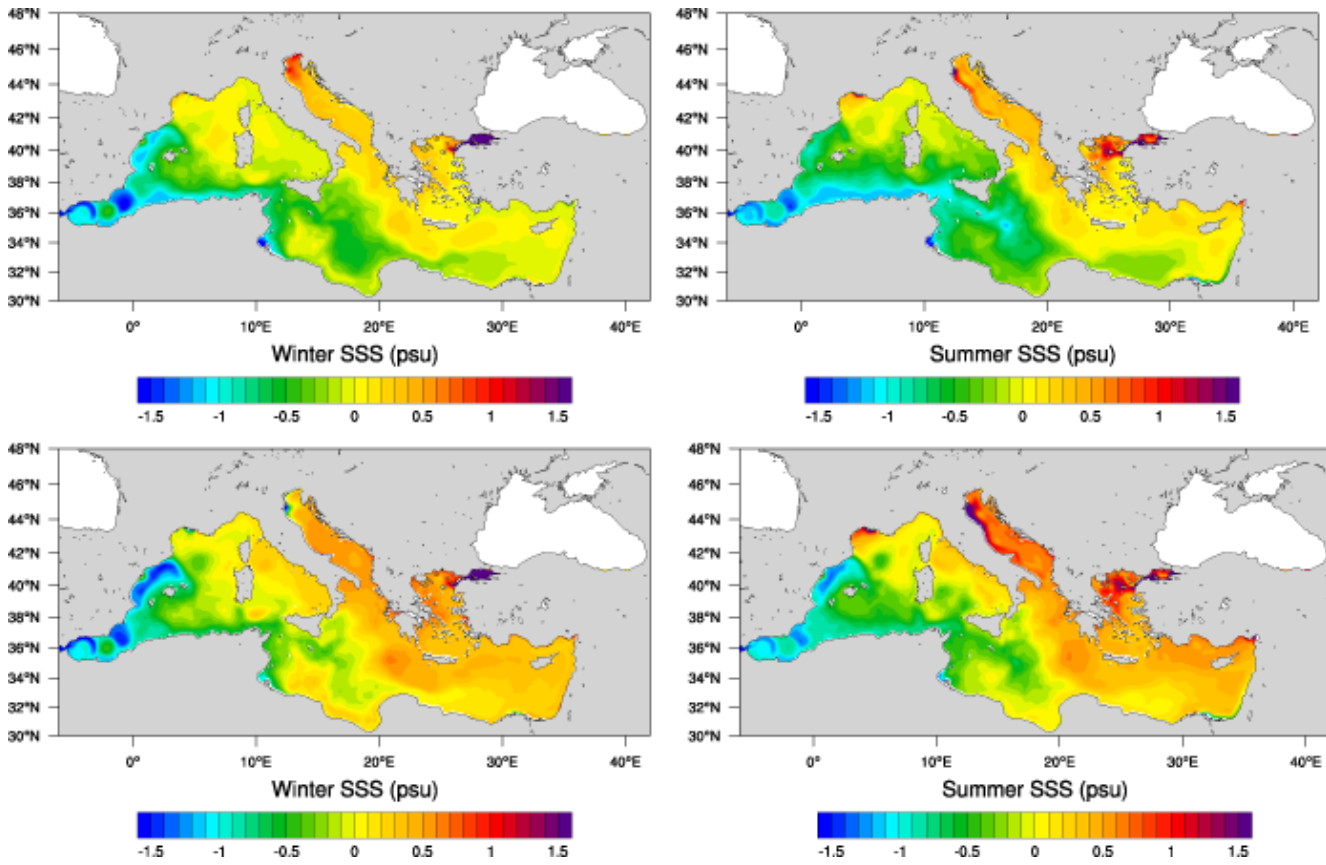


**Figure 15**

SSS difference between averages over the scenario and the historical simulations for winter (left panels) and summer (right panels). Upper panels show averages over the period 2046-2065, lower panels over the period 2081-2100 (right panel). Historical simulation has been averaged over the entire period 1981-2005

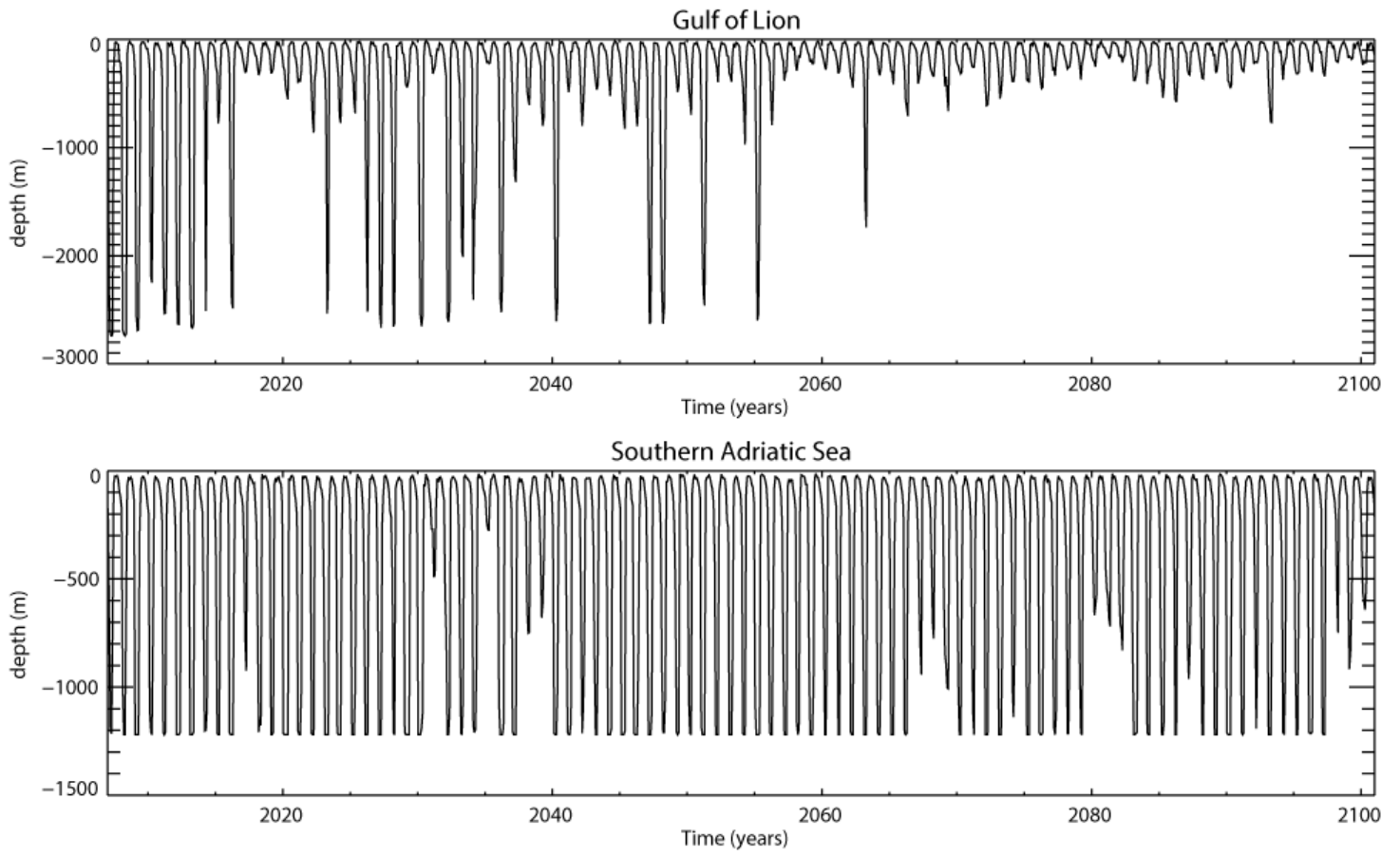


**Figure 16**

Time evolution of the monthly maximum MLD computed over the Gulf of Lion area and the Southern Adriatic Sea. Scenario simulation

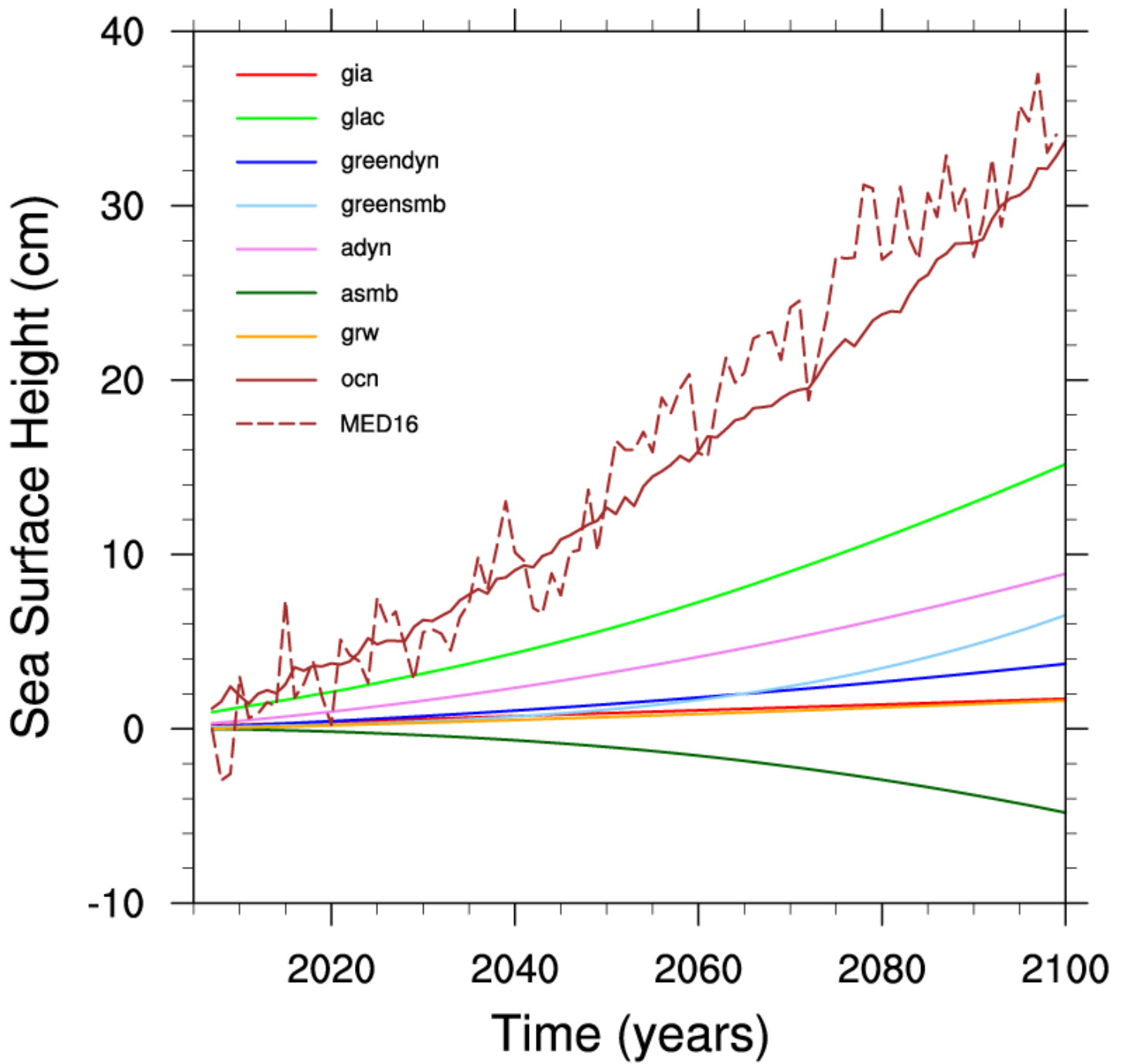


Figure 17

Time evolution of the components contributing to the projected mean sea level in the Mediterranean under the RCP8.5. Solid lines represent the central estimate over available models

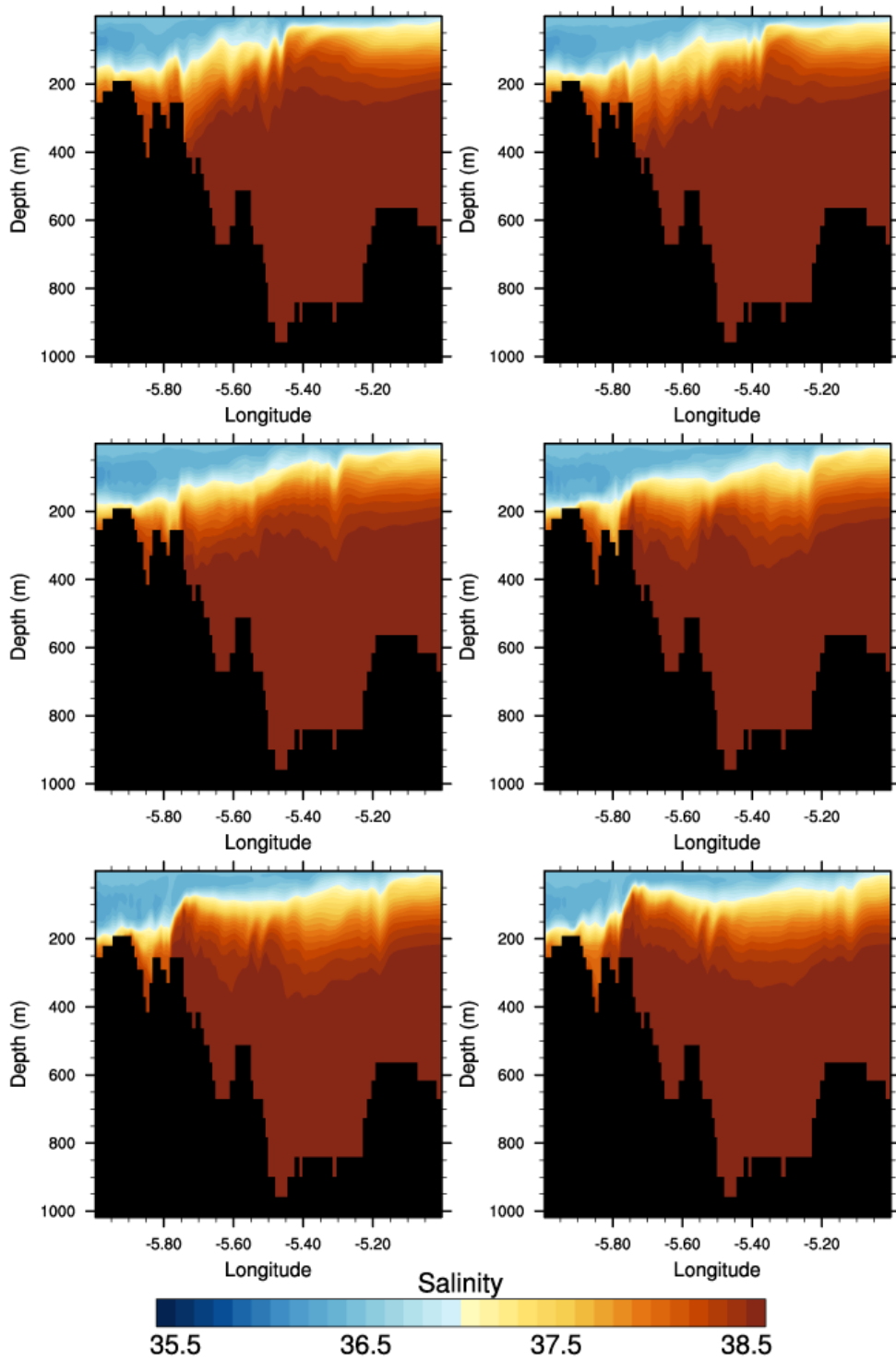
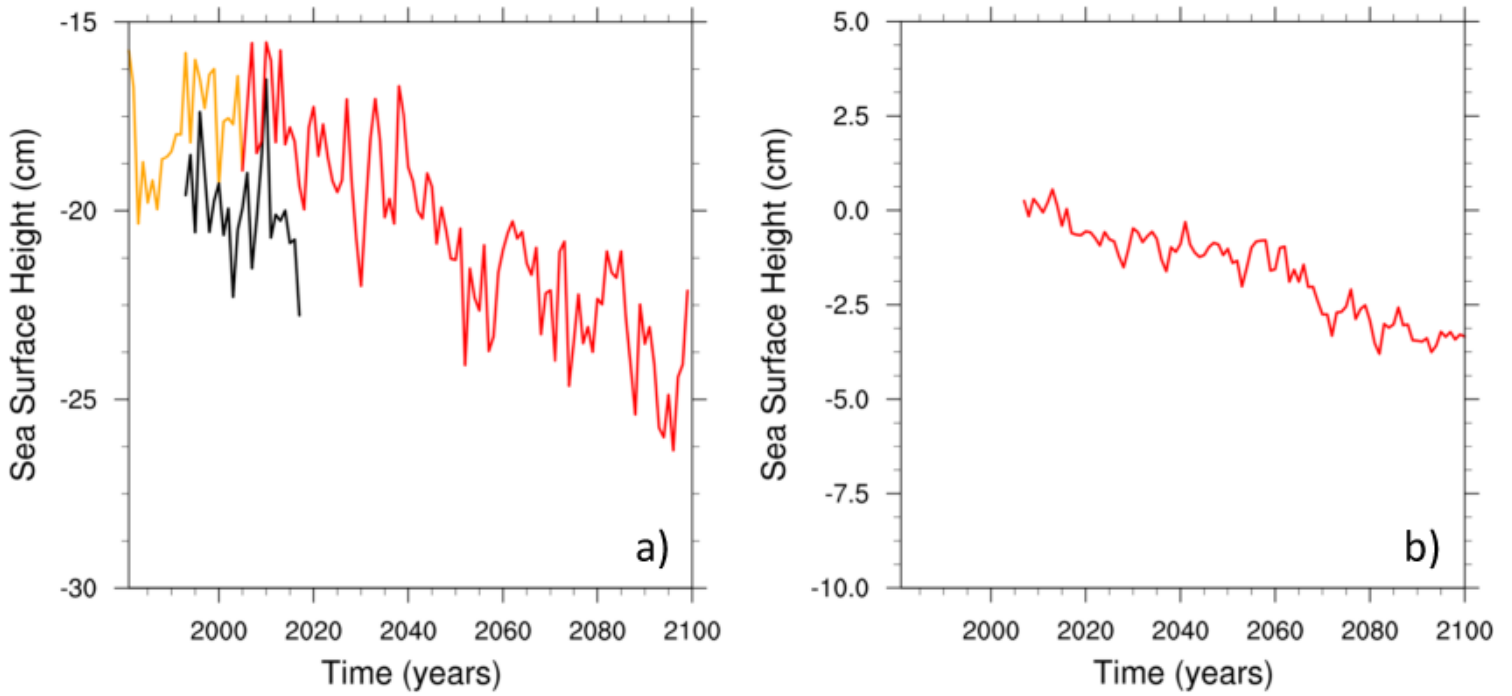


Figure 18

Evolution of salinity in a section of the Strait of Gibraltar at intervals of 1 h



**Figure 19**

Differences between values averaged over the Mediterranean basin and over the Atlantic box for the historical (orange) and scenario (red) simulations, (in black superimposed AVISO ADT) (left panel). In the right panel, the same difference for the GLOBAL dynamic sea surface height. Annual values

**Figure 20**

Difference in the MED16 stereodynamic SLC computed over the period 2046-2065 (upper panel) and over the period 2080-2099 (lower panel) relative to the historical period

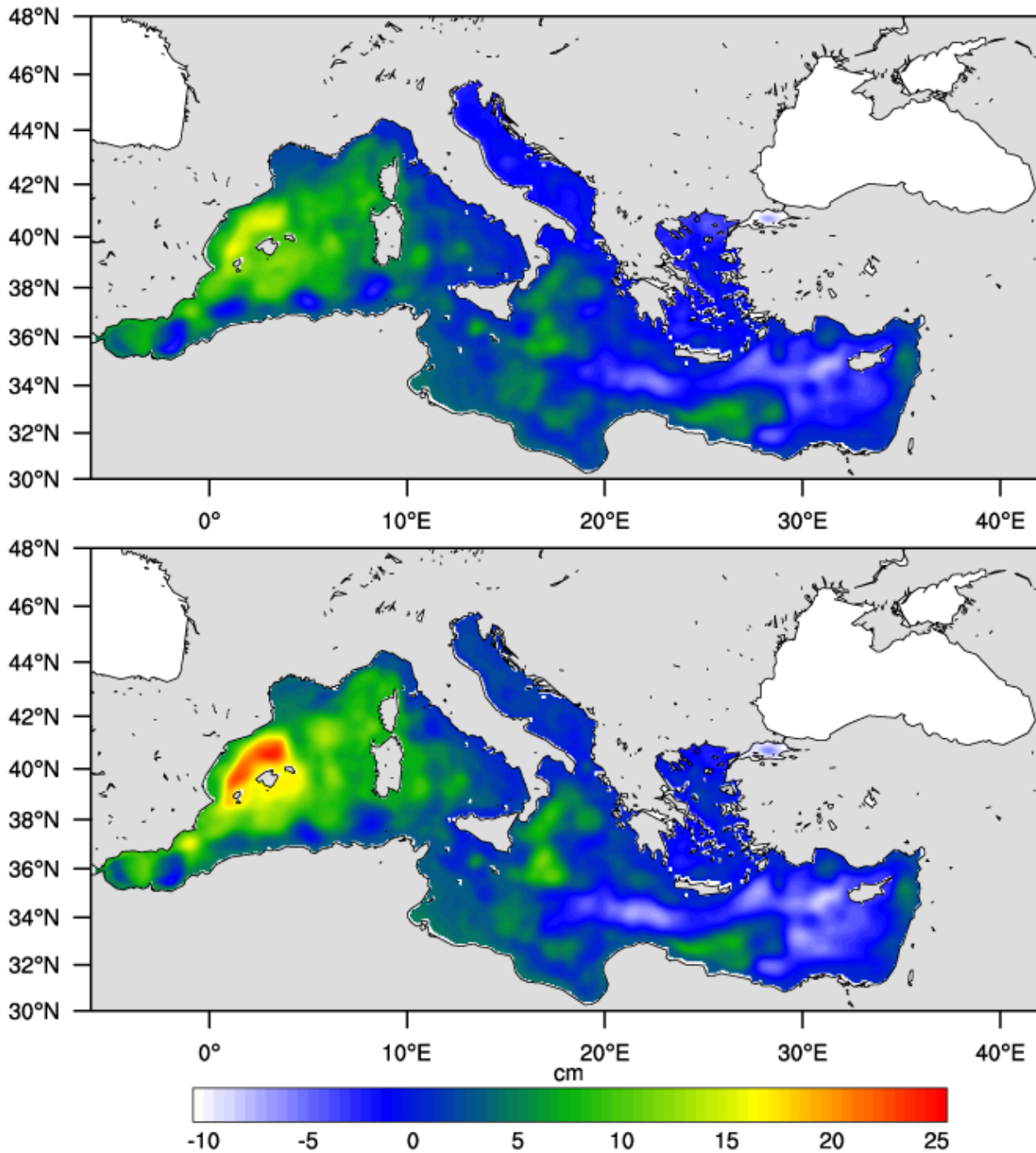


**Figure 21**

Difference in the stereodynamic SLC computed by the MED16 simulation and the ensemble mean from Slangen et al. (2014). Mean over the period 2046-2065 (upper panel), and over the period 2080-2099 (lower panel)